MATERIALS CHEMISTRY FRONTIERS

CHINESE CHEMICAL SOCIETY

ROYAL SOCIETY OF CHEMISTRY

RESEARCH ARTICLE

View Article Online
View Journal | View Issue

Check for updates

Cite this: *Mater. Chem. Front.*, 2025, **9**, 976

Gamma-induced one-step synthesis of reduced graphene oxide–silver nanoparticles with enhanced properties†

Souad Abou Zeid,*[a] Liran Hu,[a] Rasta Ghasemi,[b] Matthieu Gervais,[c] Jaspreet Kaur Randhawa,[d] Prem Felix Siril[e] and Samy Remita*[af]

Received 1st December 2024,
Accepted 27th January 2025

DOI: 10.1039/d4qm01057d

rsc.li/frontiers-materials

This study presents a novel gamma-induced one-pot synthesis of reduced graphene oxide–silver nanoparticle (rGO–Ag NPs) nanocomposites. Syntheses were conducted in a deoxygenated aqueous medium containing 0.2 g L^{-1} graphene oxide (GO), silver ions (10^{-3} or 10^{-2} mol L^{-1}), and 0.2 mol L^{-1} isopropanol at ambient temperature and pressure. Multi-technique characterization confirmed the reduction of GO and silver ions, forming nanocomposites with significantly improved physicochemical and electrochemical properties compared to pristine GO, rGO alone, and rGO–Ag NPs prepared by other methods. UV-Vis absorption spectroscopy revealed tunable optical properties, while UPS measurements provided insights into the energy band structure, highlighting interactions between rGO and Ag NPs that enhance electronic properties. XPS and ATR-FTIR confirmed the successful reduction processes. SEM–EDX analyses demonstrated uniform silver nanoparticle distribution on rGO sheets. The C/O ratio significantly increased after irradiation, with values of 10.8 and 9.6 for composites synthesized with 10^{-3} and 10^{-2} mol L^{-1} in silver ions, respectively, compared to 11.2 for rGO alone. Raman spectroscopy showed a lower intensity ratio (I_D/I_G) between D and G bands (1.18 for nanocomposites *vs.* 1.40 for rGO), indicating fewer structural defects. Improved thermal stability was evidenced by reduced weight loss (10%) at 300–800 °C. Electrochemical studies revealed exceptional specific capacitance values of 218 F g^{-1} (10^{-3} mol L^{-1} Ag^+ at 50 kGy) and 298 F g^{-1} (10^{-2} mol L^{-1} Ag^+ at 70 kGy), surpassing the 125.4 F g^{-1} for rGO alone. These findings highlight the potential of gamma-induced synthesis for producing rGO–Ag NPs nanocomposites for high-performance supercapacitor applications.

1. Introduction

Noble metal nanostructures, particularly those composed of silver (Ag) or gold (Au), have garnered significant interest due to their unique physical and chemical properties, which are intrinsically linked to their size, shape, and composition.[1–4] These properties make noble metals highly valuable in a myriad of applications, ranging from catalysis and electronics to sensors and biomedical devices.[5–9] However, the integration of noble metals with other functional materials has become an important strategy to enhance their performance and broaden their applicability.[10–12] This synergy not only enhances the performance of the individual components but may also yield novel functionalities that are critical for advanced technological applications.[13–16]

Among the materials that hold great promise for the development of noble metal-based composites, graphene and its derivatives stand out prominently. Graphene, a two-dimensional sp^2-hybridized carbon allotrope, has revolutionized materials science due to its exceptional properties, including high electron mobility, excellent mechanical stiffness, extraordinary electronic transport, and high electrical conductivity.[17–20] These characteristics position graphene as a crucial material for applications ranging from nanoelectronics and energy storage to biosensing and drug delivery.[21–26]

[a] Institut de Chimie Physique, ICP, UMR 8000, CNRS, Université Paris-Saclay, bâtiment 349, Campus d'Orsay, 15 avenue Jean Perrin, 91405 Orsay Cedex, France. E-mail: souadabouzeid321@gmail.com, samy.remita@universite-paris-saclay.fr
[b] Institut d'Alembert, IDA, ENS Paris-Saclay, 4 Avenue des sciences, 91190 Gif-sur-Yvette, France
[c] Laboratoire Procédés et Ingénierie en Mécanique et Matériaux, PIMM, Arts et Métiers ParisTech, UMR 8006, CNRS, CNAM, HESAM université, 151 boulevard de l'hôpital, 75013 Paris, France
[d] School of Mechanical and Materials Engineering, Indian Institute of Technology Mandi, Mandi 175005, Himachal Pradesh, India
[e] School of Chemical Sciences, Indian Institute of Technology Mandi, Mandi, Himachal Pradesh 175005, India
[f] Département Chimie Vivant Santé, EPN 7, Conservatoire National des Arts et Métiers, CNAM, 292 rue Saint-Martin, 75141 Paris Cedex 03, France

† Electronic supplementary information (ESI) available. See DOI: https://doi.org/10.1039/d4qm01057d

However, the scalable production of pristine graphene remains a significant challenge, driving researchers to explore alternative routes for synthesizing graphene-like materials.[27] In this context, graphene oxide (GO) and reduced graphene oxide (rGO) have emerged as viable alternatives for large-scale production and application.[28]

GO, obtained *via* the oxidation of graphite, contains various oxygen-containing functional groups, such as epoxy, hydroxyl, carbonyl, and carboxyl moieties. These functionalities play a crucial role in modifying the electronic structure of graphene while significantly enhancing GO's processability and dispersibility in various solvents.[29] This makes GO an ideal precursor for synthesizing graphene-based nanocomposites. The reduction of GO into rGO is a critical step in restoring the desirable characteristics of graphene while retaining some beneficial traits of GO that facilitate composite formation.[30] Conventional methods for reducing GO include chemical techniques employing reducing agents such as hydrazine or sodium borohydride, as well as thermal and electrochemical reduction processes.[31,32] Despite their effectiveness, these methods often present challenges, such as the use of hazardous chemicals, high energy consumption, and limitations in scalability.[33] Moreover, achieving complete reduction of GO while maintaining structural integrity and ensuring the preservation of intrinsic properties remains a formidable obstacle in the field.[27]

In our previous work,[32] we demonstrated the feasibility of using γ-ray irradiation to reduce GO through water radiolysis. This method not only proved to be efficient but also more environmentally friendly compared to conventional reduction techniques, which often rely on hazardous chemicals. However, we acknowledge that the use of γ-ray irradiation is not without its own environmental considerations, including the management of radioactive materials and the need for proper safety protocols. Despite these considerations, our study revealed that rGO produced through γ-ray irradiation exhibited a relatively high specific capacitance, indicating its significant potential for energy storage applications. Furthermore, we established an exponential correlation between capacitance and the absorbed dose of radiation, underscoring the tunability of the rGO properties through controlled irradiation. Notably, we determined that the theoretical absorbed dose required for complete reduction of 0.2 g L^{-1} GO is precisely 6 kGy (this value being contingent upon the specific characteristics of the commercial GO used in our experiments, such as oxidation rate), marking a clear benchmark for optimizing the reduction process. These findings highlighted the potential of radiolytic reduction as a scalable and effective approach for producing high-quality rGO, paving the way for its application in various graphene-based nanocomposites and advanced materials.

Building on these findings,[32] this current research focuses on the one-pot radiolytic synthesis of rGO–Ag nanocomposites. The integration of silver nanoparticles with graphene-based materials provides an opportunity to synergistically enhance the properties of both components, leading to nanocomposites with superior functionalities.[34–37] In catalytic applications, the presence of Ag NPs on the rGO surface can enhance electron transfer rates and increase the active surface area, leading to improved catalytic activity and stability.[38,39] Similarly, in sensing applications, the combination yields heightened sensitivity and selectivity for various analytes.[40,41] Furthermore, the antimicrobial properties conferred by AgNPs present potent antibacterial effects, making these nanocomposites valuable for water treatment and biomedical applications.[42,43] In energy storage, rGO–Ag nanocomposites have shown promise as electrode materials with enhanced capacitance and charge transfer capabilities.[44,45]

Traditional synthesis methods for rGO–Ag nanocomposites often rely on hazardous reducing agents. These chemical reduction processes typically entail multi-step procedures and the use of surfactants to stabilize the nanoparticles.[46,47] However, these surfactants can adversely affect the performance of the resulting composites due to their strong adsorption on the metal NPs, limiting the overall efficacy in practical applications.[30,48,49] To address these limitations, alternative techniques have been developed.[50–55] Thermal reduction and electrostatic assembly methods have shown promise, while recent studies have explored more innovative approaches. Li *et al.*[54] demonstrated a facile and rapid microwave irradiation method, and Ali Mohamed *et al.*[55] reported an eco-friendly sonication approach. These methods offer advantages such as reduced processing time and improved energy efficiency. However, challenges persist in terms of scalability, precise control over nanoparticle characteristics, and uniform dispersion of Ag NPs on the rGO surface. Moreover, these techniques may not fully meet the growing demand for sustainable and efficient synthesis methods. In this context, radiolytic synthesis emerges as an innovative alternative. Several studies have explored this approach, demonstrating its potential for producing high-quality rGO–Ag nanocomposites.[56–60] However, many existing radiolytic methods still require multiple steps or additional reducing agents, leaving room for further optimization. Additionally, detailed analysis of nanocomposite properties has been limited in previous studies.

Our research focuses on a novel radiolytic synthesis method that offers several key advantages over existing techniques. This method utilizes a one-pot, single-step process without additional reducing agents, allowing for precise control over nanoparticle size and distribution. It ensures uniform dispersion of Ag NPs on the rGO surface, offers high reproducibility and scalability potential, and provides an environmentally friendly approach with minimal waste generation. The process employs gamma-irradiation to generate reducing species directly within the reaction medium *via* water radiolysis, enabling simultaneous reduction of graphene oxide and silver ions. The reducing power of species such as hydrated electrons (e_{aq}^-), hydrogen atoms ($H^\bullet$) or isopropanol radicals, allows for precise and quantitative control over the reduction process. Moreover, gamma-irradiation produces reducing agents uniformly throughout the solution, ensuring a homogeneous initial dispersion of components—critical for achieving high monodispersity and reproducibility of formed nanostructures.[61]

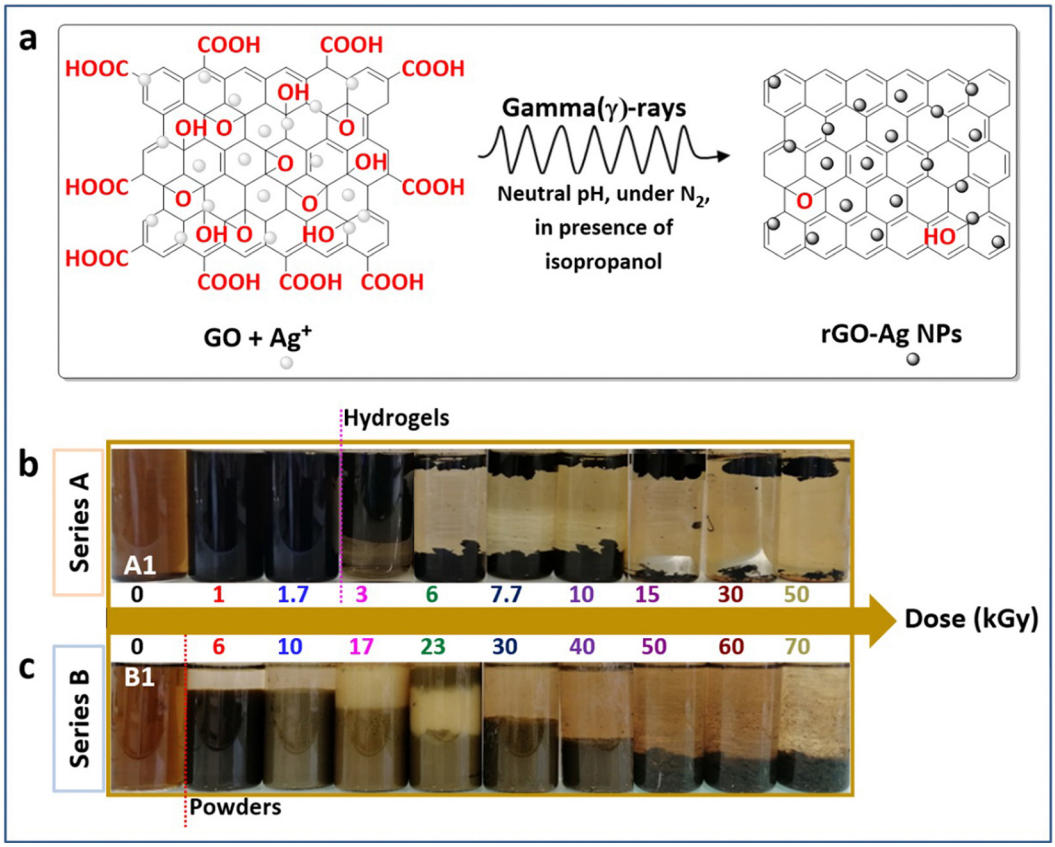

Fig. 1 Schematic representation of the radiolytic synthesis of rGO–Ag NPs in aqueous solution (a). Photographs showing the effect of increasing absorbed dose on the one-step reduction of a degassed aqueous solution containing 0.2 mol L^{-1} IPA and 0.2 g L^{-1} of GO together with $[Ag^+]_0$ = 10^{-3} mol L^{-1} (series A) (b) or $[Ag^+]_0$ = 10^{-2} mol L^{-1} (series B) (c).

Previous studies conducted in our laboratory have highlighted the benefits of the radiolytic approach compared to conventional chemical and electrochemical methods for fabricating metallic nanoparticles and conductive polymers.[61–68] In particular, in our recent work,[69] we demonstrated the efficient synthesis of rGO–Au nanocomposites using gamma irradiation, showcasing the effectiveness of this approach in producing high-quality nanomaterials. The self-regulating nature of gamma irradiation refers to its ability to generate reducing species uniformly and consistently throughout the reaction medium, enabling precise control over the reduction process without external intervention. This characteristic not only simplifies the synthesis process but also enhances the purity of the final product, making it particularly suitable for applications in catalysis, sensing, and environmental remediation.[70]

In this study, we will continue our exploration of the reduction of GO *via* radiolysis with an experimental approach involving the irradiation of aqueous solutions containing GO at a concentration of 0.2 g L^{-1}, silver ions at concentrations of either 10^{-3} or 10^{-2} mol L^{-1} (from silver perchlorate), and isopropanol at 0.2 mol L^{-1} as a radical scavenger to enhance the stability of radiolytic species (Fig. 1(a)). By varying the absorbed dose and silver ion concentration, we aim to elucidate the formation mechanism of rGO–Ag nanocomposites and optimize synthesis conditions to achieve superior physicochemical properties.

This study not only seeks to deepen the understanding of radiolytic nanocomposite synthesis but also lays the groundwork for developing advanced materials with tailored properties. By offering a simple, environmentally friendly, and scalable synthesis route, our research addresses significant challenges in the field of nanomaterial production. The insights from this work are expected to impact a wide range of sectors, including energy storage, catalysis, sensing, and water purification, ultimately bridging the gap between laboratory-scale production and practical, large-scale applications of these advanced materials.

2. Materials and methods

2.1 Materials and reagents

The synthesis of reduced graphene oxide–silver nanocomposites was conducted using a variety of commercially sourced materials. Graphene oxide, serving as the precursor for reduced graphene oxide, was obtained in aqueous dispersion at a concentration of 4 g L^{-1} ($C_xO_yH_z$, purity >95%) from Sigma Aldrich. The reduction process involved the use of anhydrous

silver perchlorate ($AgClO_4$) in a concentration of 97%, also sourced from Sigma Aldrich, which acted as the precursor for silver nanoparticles. Isopropanol (IPA) ($(CH_3)_2CHOH$, anhydrous, ≥99.5%) used at a concentration of 0.2 mol L^{-1} as a radical scavenger in the synthesis process, was also provided by Sigma Aldrich. Deionized water (DI), produced through a Millipore system with a resistivity of 18.2 MΩ cm, served as the solvent for all experimental procedures unless specified otherwise. This deionized water was utilized not only as a reaction medium but also as a reference standard during UV-Vis absorption spectroscopic measurements.

To maintain an inert atmosphere during the experiments, nitrogen gas (N_2) with a purity of ≥99.9% was employed for the degassing of the aqueous solutions; this nitrogen gas was obtained from Air Liquide. In the context of electrochemical experimentation, Nafion® 117 solution, comprising approximately 5% in a mixture of lower aliphatic alcohols and water, was utilized as a binder. Potassium hydroxide (KOH), sourced from Fisher Scientific, served as the electrolyte in the electrochemical characterizations. All chemicals were used as received, without undergoing further purification prior to experimentation.

2.2 Instrumentation of irradiation source

The irradiation source utilized in this study was a ^{60}Co γ-source. The current activity of this source at the time of experimentation was approximately 3000 Curie (Ci). This source is securely housed in a lead container, allowing for precise mechanical control in raising and lowering the source during irradiation.

Irradiation was performed within a panoramic chamber specifically designed to ensure safety and efficiency. Samples, comprised of aqueous solutions contained in glass vials, were placed on a fixed platform inside the chamber.

The intensity of the irradiation was quantified by the absorbed dose (D), which measures the amount of energy deposited in the irradiated solutions. The dose rate during the experiments was standardized at 3.3 kGy h^{-1}, ensuring precise control over the dosing process while maximizing both safety and treatment efficacy during irradiation. This value was consistently used throughout our experiments to achieve the required irradiation dose effectively.

The dose rates were accurately determined using Fricke's dosimetry, which relies on the oxidation process of Fe^{2+} to Fe^{3+}.[71,72]

2.3 Preparation of rGO–Ag nanocomposites *via* γ-irradiation

Prior to the experimental procedure, the commercial GO suspension was thoroughly shaken and allowed to stand undisturbed for 5 hours to prevent sedimentation. Subsequently, two separate 500 mL Erlenmeyer flasks were prepared, designated as flask A and flask B. Each flask contained aqueous solutions with consistent concentrations of GO (0.2 g L^{-1}) and IPA (0.2 mol L^{-1}) but with different concentrations of $AgClO_4$. In flask A, the concentration was 10^{-3} mol L^{-1}, while in flask B, it was increased to 10^{-2} mol L^{-1}.

To ensure homogeneity, the suspensions were thoroughly shaken before being transferred into two series of transparent glass vials (40 mL). Series A, corresponding to flask A, included 10 glass vials, while series B, corresponding to flask B, also comprised 10 glass vials. Each vial was sealed with septa and further protected from light exposure by wrapping them in aluminium foil due to the light sensitivity of Ag(I) silver salt.

To remove dissolved oxygen which could negatively impact the reduction process, the GO/Ag^+ suspensions underwent N_2 degassing for 20 minutes. Following the degassing process, the samples were subjected to gamma-irradiation using the ^{60}Co γ-source at a dose rate of 3.3 kGy h^{-1}. In series A, the samples were irradiated with increasing absorbed doses from 0 kGy up to a maximum of 50 kGy (samples A1 to A10, Fig. 1(b)). Meanwhile, series B samples were irradiated at doses increasing from 0 kGy to 70 kGy (samples B1 to B10, Fig. 1(c)).

The selection of absorbed doses was informed by previous studies. Our prior work indeed determined the reduction yield of the used commercial GO to be 3.3×10^{-5} g J^{-1}, establishing that a theoretical dose of approximately 6 kGy is necessary for the quantitative reduction of 0.2 g L^{-1} of this GO in water in presence of 0.2 mol L^{-1} in isopropanol. In these conditions, isopropanol molecules scavenge $H^\bullet$ and $HO^\bullet$ radicals produced from water radiolysis, leading to isopropanol radicals, $(CH_3)_2C^\bullet OH$, which act together with hydrated electrons (e_{aq}^-, also produced from solvent radiolysis) as reducing radicals.[32] Additionally, earlier research demonstrated that the reduction yield of Ag^+ ions (from silver perchlorate) was 6.2×10^{-7} mol J^{-1} in the same experimental conditions, in presence of 0.2 mol L^{-1} isopropanol. This reduction yield has been demonstrated to be the sum of the production yields of reducing species generated by water radiolysis: hydrated electrons, isopropanol radicals and potentially $H^\bullet$ radicals, depending on Ag^+ concentration.[73] To quantitatively reduce 10^{-3} or 10^{-2} mol L^{-1} of Ag^+ ions, absorbed doses of 1.7 kGy or 17 kGy were determined to be necessary, respectively. Thus, for the system containing 0.2 g L^{-1} of GO and 10^{-3} mol L^{-1} of Ag^+ (series A), the theoretical absorbed dose required was calculated to be 7.7 kGy. In contrast, for the solution containing 0.2 g L^{-1} of GO and 10^{-2} mol L^{-1} of Ag^+ (series B), the required reduction dose was calculated to be 23 kGy. These theoretical doses guided the selection of irradiation levels for the respective series studied in the present work.

After the irradiation process, the resultant products were collected through centrifugation at 7000 rpm for 15 minutes. The precipitated materials from each sample of the two series A and B were then dried in a hot air oven at 100 °C overnight to yield the dried products.

All experiments were conducted in duplicate to ensure reproducibility.

2.4 Reduction mechanisms and kinetics in radiolytic systems

Following the procedural description of the one-step gamma irradiation synthesis of rGO–Ag nanocomposites, it is essential to examine the underlying reduction mechanisms that drives this transformation. In our prior work,[32] we detailed the water

radiolysis process, describing the variety of reactive species produced under ionizing radiation and how they contribute to creating a reducing environment under controlled conditions. For the present study, which employs similar experimental parameters, these insights remain directly applicable.

In our experiments, conducted at neutral pH and under a nitrogen atmosphere in the presence of isopropanol, water radiolysis generates reactive species that establish a strong reducing environment. Indeed, hydrated electrons (e_{aq}^-) and isopropanol radicals ($(CH_3)_2C^\bullet OH$) act as reducing agents, where isopropanol not only scavenges $HO^\bullet$ oxidative radicals but also contributes to the generation of additional reducing species, thus amplifying the overall reducing capacity.[61,74,75]

The reduction of GO in environments containing e_{aq}^- and $(CH_3)_2C^\bullet OH$ reactive species proceeds through multiple pathways targeting the oxygenated functional groups on GO. Hydrated electrons are for instance particularly effective in reducing epoxide and carbonyl groups present on GO sheets into hydroxyl groups. These hydroxyl groups can then undergo further reduction, restoring the sp^2-bonded carbon structure essential for determining the material's electrical properties.

Through these reactions, the progressive deoxygenation of GO leads to the restoration of the graphitic sp^2 carbon network, crucial for applications relying on the electrical and structural properties of rGO. Meanwhile, isopropanol radicals participate in the reduction process, primarily targeting hydroxyl and carbonyl groups, IPA radicals being oxidized by hydroxyl groups into acetone.

Simultaneously, the reduction of silver ions (Ag^+) into zero-valent silver atoms (Ag^0) occurs *via* multiple pathways, including interactions with hydrated electrons, isopropanol radicals, and hydrogen atoms. These reactions are summarized as follows:[73,76,77]

$$Ag^+ + e_{aq}^- \rightarrow Ag^0 \quad (1)$$

$$Ag^+ + (CH_3)_2C^\bullet OH \rightarrow Ag^0 + (CH_3)_2CO + H^+ \quad (2)$$

$$Ag^+ + H^\bullet \rightarrow Ag^0 + H^+ \quad (3)$$

Silver atoms are thermodynamically unstable. They aggregate into silver oligomers, then into bigger silver nanoparticles, the properties of which depend on particle size.[73] Silver aggregation process can be summarized by the following reactions:

$$Ag^0 + Ag^+ \rightarrow Ag_2^+ \quad (4)$$

$$Ag_x^{p+} + Ag_y^{m+} \rightarrow Ag_{(x+y)}^{(p+m)+} \quad (5)$$

To mitigate and control aggregation, GO should serve as a stabilizing support, limiting particle growth, ensuring a uniform size distribution and enhancing the overall performances of the resulting rGO–Ag nanocomposites.

From a mechanistic point of view, it is important to consider the kinetic competition between two reduction mechanisms: the reduction of GO by e_{aq}^- and $(CH_3)_2C^\bullet OH$ on the one hand, and the reduction of Ag^+ by the reducing species on the other hand. The reduction of GO by these reducing radicals has been investigated using pulse radiolysis. The rate constants obtained are approximately $k_1 = 2.8 \times 10^7$ L g^{-1} s^{-1} for e_{aq}^- and $k'_1 = 8 \times 10^4$ L g^{-1} s^{-1} for $(CH_3)_2C^\bullet OH$.[78] It should be noted that these rate constants are expressed in L g^{-1} s^{-1} due to the unknown molar mass of GO. Also, the reduction of GO by e_{aq}^- occurs significantly faster than that by $(CH_3)_2C^\bullet OH$. Similarly, Ag^+ ions are reduced extremely rapidly by solvated electrons, with a rate constant roughly $k_2 = 3.6 \times 10^{10}$ L mol^{-1} s^{-1}.[79] Furthermore, Ag^+ can also be reduced by hydrogen atoms ($H^\bullet$), with a rate constant of $k_3 = 1.5 \times 10^{10}$ L mol^{-1} s^{-1}.[80] The contribution of $H^\bullet$ to the reduction of Ag^+ is particularly significant under the employed experimental conditions.

To compare the kinetics of GO reduction with that of Ag^+ ions, we can focus on their reactions with e_{aq}^-, which is the fastest route. Thus, we can estimate the competition ratio (R):

$$R = \frac{k_1 \times [\mathrm{GO}] \times \left[e_{aq}^-\right]}{k_2 \times [Ag^+] \times \left[e_{aq}^-\right]} \quad (6)$$

where [GO] is the concentration of GO in g L^{-1}, [Ag^+] is the concentration of silver ions in mol L^{-1}, k_1 is the rate constant for the reduction of GO in L g^{-1} s^{-1}, and k_2 is the rate constant for the reduction of silver ions in L mol^{-1} s^{-1}.

This competition kinetics highlights the importance of carefully tuning reaction conditions, *inter alia*, by adjusting GO and Ag^+ initial concentrations, to achieve optimal outcomes in the synthesis of rGO–Ag hybrid materials.

2.5 Characterization of rGO–Ag nanocomposites

The radiosynthesized materials were characterized using a comprehensive suite of analytical techniques to evaluate their chemical, optical, electronic, structural, morphological, thermal, and electrochemical properties. These analyses provide crucial insights into the formation, composition, and functionality of the materials, which are essential for their potential applications. All experiments were conducted in duplicate to ensure reproducibility.

UV-Vis absorption spectroscopy was employed to investigate the evolution of GO and Ag^+ concentrations in irradiated samples as a function of absorbed dose. This technique provided insights into the nature of the bonds and functional groups present, as well as their physicochemical and optical properties. Additionally, UV-Vis absorption spectroscopy allowed the determination of the band gap of synthesized hybrid material within each sample, confirming the reduction of GO into rGO and the conversion of Ag^+ ions into Ag NPs. Absorption spectra were recorded using an Agilent/HP 8453 UV-Vis spectrophotometer over the wavelength range of 200–800 nm, with distilled water serving as a reference. Measurements were conducted immediately after gamma-irradiation, with a dilution factor of 10 applied to the second series of samples (series B) initially containing 0.2 g L^{-1} GO, 10^{-2} mol L^{-1} $AgClO_4$, and 0.2 mol L^{-1} IPA.

Fourier transform infrared spectroscopy-attenuated total reflectance (FTIR-ATR) was utilized to examine the functional groups present in both irradiated and non-irradiated samples.

The powdered samples were analyzed using a Bruker Vertex 70 spectrometer. They were placed on a diamond crystal attached to an ATR plate (Pike MIRacle™ crystal plate diamond/ZnSe) and scanned in the range of 4000–600 cm^{-1} using a mercury cadmium telluride (MCT) detector integrated with a liquid nitrogen cooling system for enhanced sensitivity. This characterization was vital for identifying changes in functional groups that occurred during irradiation.

Raman spectroscopy was employed to analyze the structural transformation of GO into rGO and the formation of rGO-based nanocomposites. Samples were prepared by depositing 20 μL of aqueous suspension onto indium tin oxide (ITO) substrates, followed by spin coating at 3000 rpm for 30 seconds and drying at 100 °C for 10 minutes. Raman spectra were recorded using a Horiba Lab RAM HR Evolution system with a 532 nm laser, set to a power of 1 mW, and focused with a 50× objective lens (0.5 NA). Analyzing the spectra in the range of 200–2000 cm^{-1} allowed the confirmation of changes in hybridization states and the crystalline quality of the synthesized materials.

X-ray photoelectron spectroscopy (XPS) and ultraviolet photoelectron spectroscopy (UPS) were carried out on thin films prepared on ITO substrates following the same preparation conditions as for Raman analysis. The XPS measurements were conducted using a Thermo Scientific NEXSA Surface Analysis System with a monochromatic Al Kα X-ray source (1486.6 eV) and a spherical analyzer. The data were analyzed with Thermo Scientific Avantage software. For UPS, He I radiation ($h\nu$ = 21.22 eV) was used to probe the valence bands, providing insights into the electronic properties and surface characteristics of the materials.

Scanning electron microscopy (SEM) was utilized to observe the morphology of the synthesized materials using a HITACHI S3400N-IDA system. This technique was supplemented by energy dispersive X-ray spectroscopy (EDX) to assess the elemental composition. Samples were prepared by depositing a small quantity of solid material onto a carbon support. EDX analysis facilitated qualitative and quantitative assessments of the elemental constituents, collecting signals from defined areas imaged by SEM to yield average concentration values for each detected element.

Thermogravimetric analysis (TGA) was performed using a TGA Q500 (TA Instruments, USA) to evaluate the thermal stability and composition of the materials. The analysis was conducted under an oxygen flow rate of 60 mL min^{-1}, covering a temperature range from 22 °C to 900 °C at a heating ramp rate of 10 °C min^{-1}.

Cyclic voltammetry (CV) measurements were conducted using a Metrohm Autolab potentiostat equipped with Nova software to assess the electroactivity of the synthesized materials. For the electrochemical experiments, a conventional three-electrode cell configuration was utilized, employing an Ag/AgCl reference electrode, a platinum counter electrode, and a glassy carbon (GC) working electrode with a diameter of 3 mm and a surface area of 0.07 cm^2. Prior to use, the working electrodes were polished using SiC-paper and thoroughly rinsed with ultrapure water (18.2 MΩ cm). The preparation of the samples involved utilizing 180 μL of a 0.2 g L^{-1} aqueous solution, to which 20 μL of Nafion was added as a binder. A 10 μL solution of each sample was then drop-casted onto the GC working electrode and allowed to dry slowly under ambient conditions. During the electrochemical measurements, a 0.1 M KOH aqueous electrolyte was utilized within a voltage range of −0.4 V to +0.4 V, with varied scan rates ranging from 10 to 200 mV s^{-1}. This characterization aimed to calculate the specific capacitance of the samples, contributing to the understanding of their potential applications in energy storage.

2.6 Electronic and electrochemical characterization methods

2.6.1 Band gap determination. The optical band gap (E_g) of the materials was determined using the Tauc method, which relates the energy gap to the absorption coefficient (α) through the Tauc relation:[81]

$$(\alpha h\nu)^r = A(h\nu - E_g) \tag{7}$$

where: A is a material-dependent constant, $h\nu$ represents the photon energy, with $h\nu = hc/\lambda$, λ being the wavelength of incident light, α is the absorption coefficient, r reflects the nature of electronic transitions between the valence and conduction bands (for direct allowed transitions, r = 1/2; for indirect allowed transitions, r = 2).

For an indirect transition semiconductor, as in the case of the synthesized nanocomposites, E_g was obtained by plotting $(\alpha h\nu)^2$ against $h\nu$ and extrapolating the linear portion of the plot near the absorption onset.

Physical constants used in these calculations include:

– Speed of light: $c = 3 \times 10^8$ m s^{-1}

– Planck's constant: $h = 6.63 \times 10^{-34}$ J s

– Elementary charge: $e = 1.6 \times 10^{-19}$ C

2.6.2 Energy band diagram construction. Using ultraviolet photoelectron spectroscopy (UPS), we determined the maximum of the valence band (VB_{max}), as well as the work function (WF), to analyze the electronic properties near the Fermi level, essential for understanding material properties like conductivity and semiconducting behavior.

Key definitions and calculations:

– Fermi level (E_F): the highest occupied energy level by electrons at 0 K, situated within the conduction band in metals and in the band gap for semiconductors and insulators.

– Work function (WF): defined as the minimum energy required to move an electron from the Fermi level to the vacuum level (Nv), calculated as:

$$\mathrm{WF} = \mathrm{Nv} - E_F \tag{8}$$

For semiconductors, the electron affinity (χ) is used in place of

WF, calculated as:

$$\chi = \mathrm{Nv} - \varepsilon\mathrm{C} \tag{9}$$

where εC represents the conduction band minimum energy.

From UPS data, we identified the electron cutoff energy $E_{cut\text{-}off}$ and calculated WF as:

$$\mathrm{WF} = 21.22\ \mathrm{eV} - E_{\text{cut-off}} \tag{10}$$

With values of VB_{max} and WF, the valence band energy (VB) is given by:

$$\mathrm{VB} = \mathrm{VB}_{max} + \mathrm{WF} \tag{11}$$

Using the previously calculated band gap, the conduction band energy (CB) was determined as:

$$\mathrm{CB} = \mathrm{VB} - E_g \tag{12}$$

2.6.3 Specific capacitance determination. To evaluate the electrochemical performance of the nanocomposites, the specific capacitance was derived from the cyclic voltammetry measurements. By integrating the area under the CV curve over a specified potential range, it is possible to quantify the energy storage capacity. The specific capacitance calculation reflects the material's charge–discharge characteristics, redox behavior, and efficiency in energy storage applications. Ideally, a supercapacitor's CV curve presents a rectangular shape, which signifies low internal resistance and favorable electrochemical properties.

The specific capacitance (C_{sp}) was calculated using the following equation:

$$C_{sp} = \frac{\int_{E_1}^{E_2} i(E)\mathrm{d}E}{(E_2 - E_1) \times m \times v} \tag{13}$$

where: C_{sp} is the specific capacitance in F g^{-1}, $E_2 - E_1$ represents the potential range in the CV measurements (V), m is the mass of the active material on the working electrode (g), v is the scan rate (V s^{-1}), $\int_{E_1}^{E_2} i(E)\mathrm{d}E$ is the integrated voltammetric charge.

3. Results and discussions

3.1 Visual characterization and kinetic studies

The visual results from the sample of both series, A and B, before and after gamma irradiation at varying absorbed doses, are presented in Fig. 1(b) and (c), respectively. Post-irradiation visual assessments revealed pronounced alterations in color and morphology. Initially, both samples corresponding to series A (A1) and series B (B1) exhibited a characteristic brown hue, attributed to the mixture of colorless silver ions and brown colored graphene oxide. However, a significant change in color was detected upon irradiation, even at the lowest absorbed doses.

In series A (Fig. 1(b)), the irradiation effects mirrored established behaviors of GO. Between absorbed doses of 1 and 3 kGy, the solution maintained a uniform dark appearance, indicative of the onset of reduction activity. An increase in the absorbed dose from 3 to 6 kGy facilitated the emergence of visible hydrophobic aggregates at the surface, culminating in sedimentation at higher doses. This enhancement in hydrophobicity correlates with a marked reduction in oxygen-containing functional groups on the GO, including –OH, –COOH, and epoxy groups, which are known to increase hydrophilicity *via* hydrogen bonding. As highlighted in our previous works, the gradual depletion of these groups under irradiation enhances hydrophobic interactions and re-establishes π–π stacking ones among the aromatic rings of GO, thus fostering aggregate formation as the absorbed dose surpassed 6 kGy. Notably, the reduction of silver ions at a concentration of 10^{-3} mol L^{-1} over a range of 1.7 kGy in series A was not distinctly observable, complicating the assessment of whether the reduction of silver ions outpaced that of GO.

Conversely, series B exhibited more pronounced color changes from the outset of irradiation. As shown in Fig. 1(c), transition to a grayish suspension occurred, with sedimentation becoming increasingly evident at elevated irradiation levels. Between 17 and 23 kGy, the formation of hydrophobic aggregates at the surface was observed, eventually leading to their settling at the bottom of the sample. This behavior indicates that the higher concentration of silver ions in series B (10^{-2} mol L^{-1}) facilitated a more rapid reduction compared to GO. Specifically, complete reduction of silver ions occurred around 17 kGy, establishing a pivotal threshold at which significant reduction of GO commenced.

To quantitatively assess the kinetic processes across both series, the competition ratio R was calculated using eqn (6) derived in Section 2.4. The results from the experimental series are as follows:

– For series A:

$$R = \frac{2.8 \times 10^7 \times 0.2}{3.6 \times 10^{10} \times 10^{-3}} = 0.15 \tag{14}$$

– For series B:

$$R = \frac{2.8 \times 10^7 \times 0.2}{3.6 \times 10^{10} \times 10^{-2}} = 0.015 \tag{15}$$

These calculated values indicate that in series A, the reduction of silver occurs approximately seven times faster than that of GO, while in series B, the rate is about seventy times faster. This trend explains and validates the visual data presented in Fig. 1(b), which demonstrates that the reduction of GO becomes evident only after the complete reduction of silver ions (17 kGy).

From these initial findings, it can be concluded that rGO–Ag NPs composites have been successfully synthesized in a single experimental process. It is crucial to determine whether these rGO–Ag NP composites produced *via* radiolysis exhibit properties that are distinct from those of the individual components. Moreover, an exploration of how variations in absorbed dose and silver concentration influence the optical, electronic, structural, thermal, and capacitive properties of the radiosynthesized materials is essential. A comparative analysis of these properties with those of rGO–Ag NPs composites synthesized through alternative methods reported in the literature will provide valuable insights into the efficacy and uniqueness of this synthesis approach. These aspects will be systematically addressed in the subsequent sections.

3.2 UV-Vis absorption spectroscopy characterization

The UV-Vis spectra of samples from series A and B were systematically recorded before and after gamma-irradiation, as depicted in Fig. 2(a) and (b). These spectral analyses revealed significant alterations that correlate with the absorbed dose, providing critical insights into the reduction mechanisms of GO and silver ions. Initially, the absorption spectra for the unirradiated samples, A1 (0 kGy) and B1 (0 kGy), exhibited two

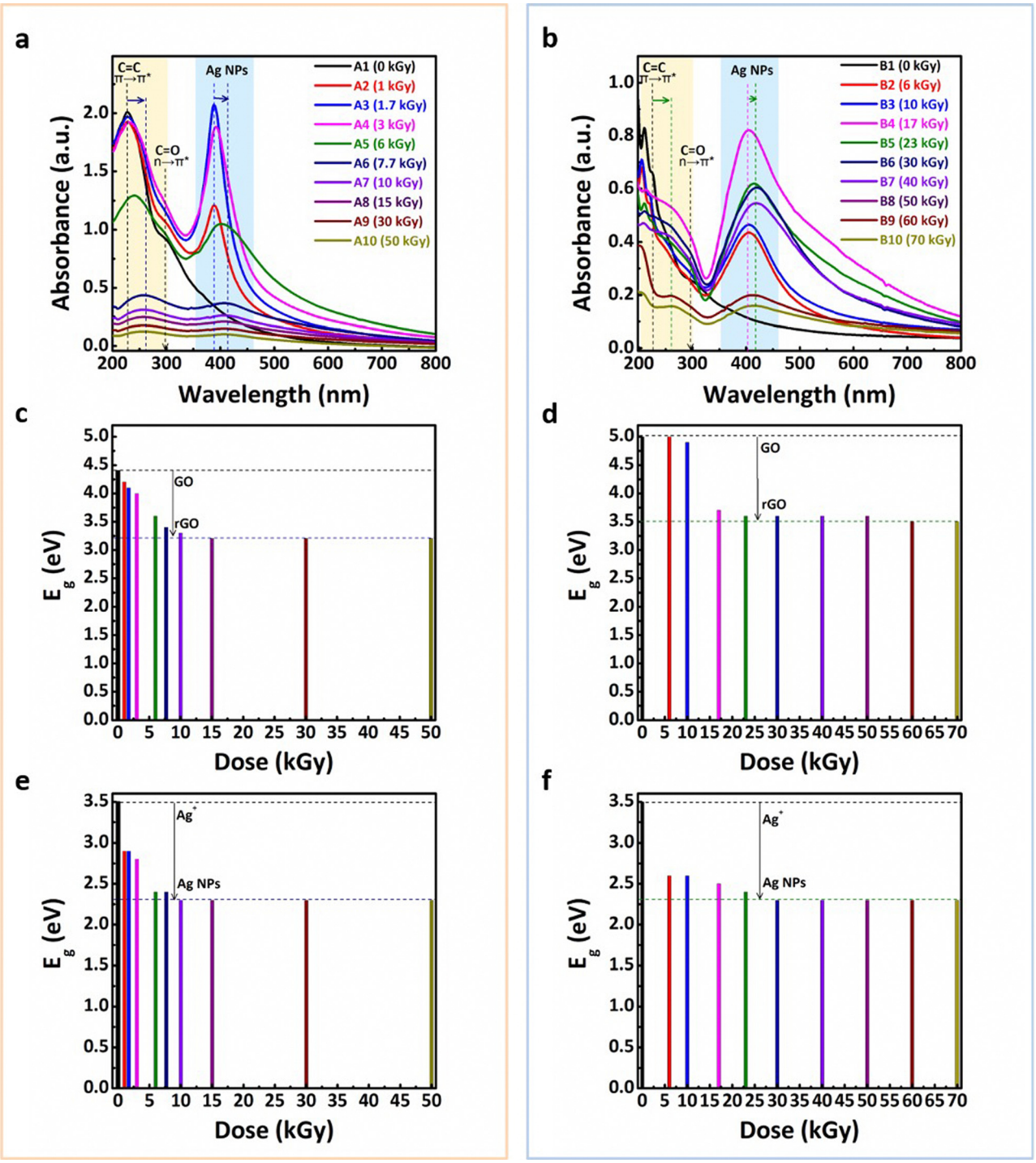

Fig. 2 UV-Vis monitoring of the radiolytic reduction of a solution containing GO (0.2 g L^{-1}) in the presence of isopropanol (0.2 mol L^{-1}) and $[Ag^+]_0$ = 10^{-3} mol L^{-1} (series A) (a) or $[Ag^+]_0$ = 10^{-2} mol L^{-1} (series B) (b), diluted tenfold. Reference: ultrapure water. Optical pathlength: 0.2 cm. Evolution of the energy gap (eV) as a function of the absorbed dose for series A (c) and series B (d). Experimental uncertainty for repeated measurements is less than 5%. Evolution of the energy gap (eV) of silver nanoparticles as a function of the absorbed dose for series A (e) and series B (f). The margin of error for the obtained values is less than 5%.

distinct broad bands characteristic of GO: the first one centered around 230 nm, attributed to $\pi \rightarrow \pi^*$ electronic transitions within the aromatic C═C bonds indicative of the graphitic structure, and the other one at approximately 295 nm, which corresponds to $n \rightarrow \pi^*$ transitions associated with carbonyl C═O functional groups.[82] These spectral features establish a baseline for subsequent observations during the reduction process.

Upon initiating gamma-irradiation, a marked increase in the intensity of the plasmon band which characterizes silver NPs was observed, reaching a peak at approximately 400 nm. This peak emerged and reached a maximum at an absorbed dose of 1.7 kGy for series A (Fig. 2(a)) and 17 kGy for series B (Fig. 2(b)), confirming the faster reduction of silver ions compared to that of GO, as already presumed (see *R* values) and in agreement with the visual observations (Fig. 1). The emergence of this plasmon band is pivotal as it indicates the conversion of Ag^+ ions into Ag NPs, which is characterized by surface plasmon resonance (SPR). The physics of metallic nanoparticles dictates that when exposed to incident light, the free conduction electrons oscillate in response to the electric field of the light wave, creating a resonant condition known as SPR. For spherical silver nanoparticles, this resonance typically occurs within the wavelength range of 350–500 nm, peaking around 410 nm.[83–85]

As the absorbed dose increased, a notable red shift of the C═C transition band from 230 nm to 265 nm was recorded at doses of 7.7 kGy for series A and 23 kGy for series B, these absorbed doses being the theoretical doses required for complete reduction of both GO and silver ions. This red shift is indicative of the effective reduction of GO to rGO, highlighting a structural transformation that enhances the electronic and optical properties of the material. Concurrently, a substantial decrease in absorbance at 295 nm was observed, which reflects the diminishing concentration of C═O groups, further confirming the reduction of GO.[86–89]

Importantly, once the reduction of silver ions was considered complete at 1.7 kGy for series A and 17 kGy for series B, sedimentation of nanoparticle suspensions was noted. This phenomenon led to irreversible aggregation of the formed nanomaterials and a subsequent decrease in the absorbance for both Ag NPs (evidenced by reduced intensity of the plasmon band) and GO (indicated by decreased absorbance at 230–265 nm and at 295 nm). This sedimentation complicates the quantification of the reduction yield of GO at 295 nm, a challenge not encountered in prior studies.[32] The spectral characteristics of the plasmon absorption band displayed intriguing differences between the two series. For series A, the plasmon band appeared symmetrical around 390 nm, indicative of relatively uniform nanoparticle size, while in series B, the plasmon band exhibited asymmetry with a peak at around 410 nm, suggesting the presence of larger and potentially more polydisperse nanoparticles. This observation emphasizes the critical role that silver ion concentration plays in determining nanoparticle morphology and size distribution.

The UV-Vis spectral analysis demonstrates the concomitant formation of predominantly spherical silver nanoparticles alongside rGO sheets throughout the irradiation process. The optimal theoretical absorbed dose for synthesizing hybrid rGO–Ag NPs, when [GO] = 0.2 g L^{-1} and $[Ag^+] = 10^{-3}$ mol L^{-1} (series A), is identified as 7.7 kGy, whereas for $[Ag^+] = 10^{-2}$ mol L^{-1} (series B), the required absorbed dose escalates to 23 kGy. Notably, the increase in Ag^+ concentration from 10^{-3} to 10^{-2} mol L^{-1} did not significantly alter the kinetics of silver reduction or the overall nanoparticle morphology; however, it did result in a marked increase in the size and a broader size distribution of the resulting metallic structures. These findings collectively highlight the efficiency of gamma-irradiation as a versatile method for producing rGO–Ag NP hybrids, illustrating the ability to fine-tune their morphological and optical properties through careful manipulation of absorbed doses and silver ion concentrations.

Furthermore, leveraging the UV-Vis data illustrated in Fig. 2(a) and (b), the band gap values of all samples were determined. The energy gaps were extracted from the absorption data using Tauc plots, where the intersection with the *x*-axis indicates the energy gap for each sample. Tauc plots for series A and B are provided in Fig. S1 and S2 (ESI†). Fig. 2(c) and (d) demonstrate the evolution of the energy gap of the starting materials (GO–Ag^+) as a function of the absorbed dose for both series. For series A (Fig. 2(c)), the energy gaps of the samples, E_g, including both non-irradiated and irradiated conditions, range from 4.4 eV to 3.1 eV. Notably, E_g value decreases significantly with increasing absorbed dose, reaching a value of 3.1 eV at an absorbed dose of 7.7 kGy, which coincides with the completion of the reduction process of both GO and Ag^+ ions. Beyond this absorbed dose, at 10 kGy and higher, the energy gap value stabilizes at 3.1 eV. In contrast, for series B (Fig. 2(d)), the energy gaps span from 5.0 eV to 3.6 eV. A pronounced reduction in E_g value is observed up to approximately 23 kGy, an absorbed dose that theoretically corresponds to the complete reduction of silver ions and GO. Beyond this point, E_g value reaches a plateau around 3.6 eV. Importantly, the energy gap for series B, which features a higher concentration of Ag^+ ions, is greater than that observed for series A.

The band gap energy of semiconducting silver nanoparticles depends on the size of the nanoparticles. For an indirect band gap, the literature estimates the band gap energy to range between 2.8–3.5 eV.[90–93] As shown in Fig. S1 and S2 (ESI†), the data from this study reveal a distinct leftward shift in the band gap with increasing absorbed dose, suggesting a size-related impact on the electronic properties. To further investigate this trend, the energy gap data are summarized in Fig. 2(e) (series A) and Fig. 2(f) (series B) as a function of absorbed dose. Both series A and B show an initial energy gap of 3.5 eV at 0 kGy, with a final energy gap consistently recorded at 2.3 eV after irradiation. This indicates that while Ag^+ ions concentration has minimal effect on the energy gap of the Ag NPs, it does influence the final energy gap in the nanocomposites, which are 3.1 eV for series A and 3.6 eV for series B, as it will be summarized in Tables 1–3.

Table 1 Values required for the calculation of the energy band structure of the GO (0.2 g L^{-1})–Ag^+ (10^{-3} mol L^{-1}) samples, both unirradiated and irradiated at various absorbed doses (series A). The uncertainty associated with the repeated experimental values is less than 5%

Series A						
Samples	E_g (eV)	VB_{max} (eV)	$E_{cut\text{-}off}$ (eV)	WF (eV)	VB (eV)	CB (eV)
A1 (0 kGy)	4.4	2.0	16.2	5.0	7.0	2.6
A2 (1 kGy)	4.2	2.1	16.3	4.9	7.0	2.8
A3 (1.7 kGy)	4.0	2.1	16.3	4.9	7.0	3.0
A4 (3 kGy)	3.8	2.1	16.3	4.9	7.0	3.2
A5 (6 kGy)	3.5	2.1	16.3	4.9	7.0	3.5
A6 (7.7 kGy)	3.3	2.1	16.4	4.8	6.9	3.6
A7 (10 kGy)	3.2	2.2	16.5	4.7	6.9	3.7
A8 (15 kGy)	3.1	2.2	16.5	4.7	6.9	3.8
A9 (30 kGy)	3.1	2.2	16.5	4.7	6.9	3.8
A10 (50 kGy)	3.1	2.2	16.5	4.7	6.9	3.8

Table 2 Values required for the calculation of the energy band structure of the GO (0.2 g L^{-1})–Ag^+ (10^{-2} mol L^{-1}) samples, both unirradiated and irradiated at various absorbed doses (series B). The uncertainty associated with the repeated experimental values is less than 5%

Series B						
Samples	E_g (eV)	VB_{max} (eV)	$E_{cut\text{-}off}$ (eV)	WF (eV)	VB (eV)	CB (eV)
B1 (0 kGy)	5.0	2.0	16.1	5.1	7.1	2.1
B2 (6 kGy)	5.0	2.1	16.2	5.0	7.1	2.1
B3 (10 kGy)	4.8	2.1	16.4	4.8	6.9	2.1
B4 (17 kGy)	3.8	2.2	16.5	4.7	6.9	3.1
B5 (23 kGy)	3.7	2.2	16.6	4.6	6.8	3.1
B6 (30 kGy)	3.7	2.3	16.7	4.5	6.8	3.1
B7 (40 kGy)	3.6	2.4	16.8	4.4	6.8	3.2
B8 (50 kGy)	3.6	2.5	16.9	4.3	6.8	3.2
B9 (60 kGy)	3.6	2.5	16.9	4.3	6.8	3.2
B10 (70 kGy)	3.6	2.5	16.9	4.3	6.8	3.2

3.3 UPS spectroscopy analysis and band diagram determination

After determining the energy gap values, it is essential to explore how absorbed doses influence the electronic properties of the rGO–Ag composites. In particular, the work function, conduction band, valence band, and Fermi level will be examined as a function of the absorbed dose for samples of both series A and B. These properties are pivotal in understanding the behavior of the composites, particularly their electronic and catalytic characteristics, under varying irradiation conditions.

Before analyzing the evolution of these properties, it is important to note that the work function of Ag, like other metals, has been determined experimentally by various methods, including photoemission measurements, thermionic emission, and contact potential measurements.[94–96] These techniques allowed the precise characterization of WF, which is critical in understanding the surface electronic properties of metals and their interaction with surrounding materials.

For silver, the reported WF value is approximately 4.3 eV.[97] While this value is well established for bulk silver, changes in the WF can occur when silver is in nanoparticle form. It has been shown that the work function of nanoparticles, particularly those with diameters smaller than 20 nm, increases as their size decreases.[98] Additionally, the interaction between Ag NPs and rGO substrate in rGO–Ag NPs composites may further influence the WF, a phenomenon that has not been extensively studied in the context of synthesized silver nanoparticle composites. This interaction, along with the irradiation-induced changes, is a key focus of the present study.

To investigate these interactions, UPS was employed to study the work function of irradiated and non-irradiated GO in the presence of silver ions at concentrations of 10^{-3} and 10^{-2} mol L^{-1}. The UPS spectra for both series of samples (A and B) are shown in Fig. S3 and S4 (ESI†). The spectra were obtained using He I radiation ($h\nu$ = 21.21 eV), and the values of VB_{max} and $E_{cut\text{-}off}$ were extracted for analysis.

In Fig. 3(a), the UPS spectra for samples A1 (0 kGy), A6 (7.7 kGy), and A10 (50 kGy) from series A are presented, while in Fig. 3(b), the UPS spectra for samples B1 (0 kGy), B5 (23 kGy), and B10 (70 kGy) from series B are shown.

In the first series (A) (Fig. 3(a)), UPS spectra revealed a spectral shift to the left with increasing absorbed dose up to 7.7 kGy. However, at higher absorbed doses, the values of VB_{max} and $E_{cut\text{-}off}$ remained constant, stabilizing at 2.2 eV and 16.5 eV, respectively. This trend indicates that the modification of the work function reaches a plateau after a certain absorbed dose, reflecting a saturation of changes in the electronic structure of the composites. The apparent work function of the rGO–Ag NPs composites also remained stable despite further irradiation, indicating that the particle size and the interaction with rGO are dominant factors in determining the work function at higher absorbed doses.

A similar shift was observed for the second series (B) (Fig. 3(b)) with an absorbed dose of 7.7 kGy, after which the VB_{max} and $E_{cut\text{-}off}$ values again stabilized at 2.2 eV and 16.5 eV. Notably, despite differences in the initial silver ion concentration (10^{-3} mol L^{-1} *versus* 10^{-2} mol L^{-1}), the final values of VB_{max} and $E_{cut\text{-}off}$ were identical for all samples at the highest absorbed doses. This suggests that the concentration of silver

Table 3 Comparative study on the electronic effect of the association of silver nanoparticles at different Ag^+ concentrations (10^{-3} mol L^{-1} and 10^{-2} mol L^{-1}) with rGO

Samples	E_g (eV)	VB_{max} (eV)	WF (eV)	VB (eV)	CB (eV)
GO (0.2 g L^{-1})–Ag^+(0 mol L^{-1}) at 0 kGy	4.4	1.3	4.9	6.2	1.8
rGO–Ag^+(0 mol L^{-1}) at 50 kGy	3.3	1.7	4.3	6.0	2.7
A1 (0 kGy): GO (0.2 g L^{-1})–Ag^+(10^{-3} mol L^{-1})	4.4	2.0	5.0	7.0	2.6
A10 (50 kGy): rGO–Ag NPs	3.1	2.2	4.7	6.9	3.8
B1 (0 kGy): GO (0.2 g L^{-1})–Ag^+(10^{-2} mol L^{-1})	5.0	2.0	5.1	7.1	2.1
B10 (70 kGy): rGO–Ag NPs	3.6	2.5	4.3	6.8	3.2

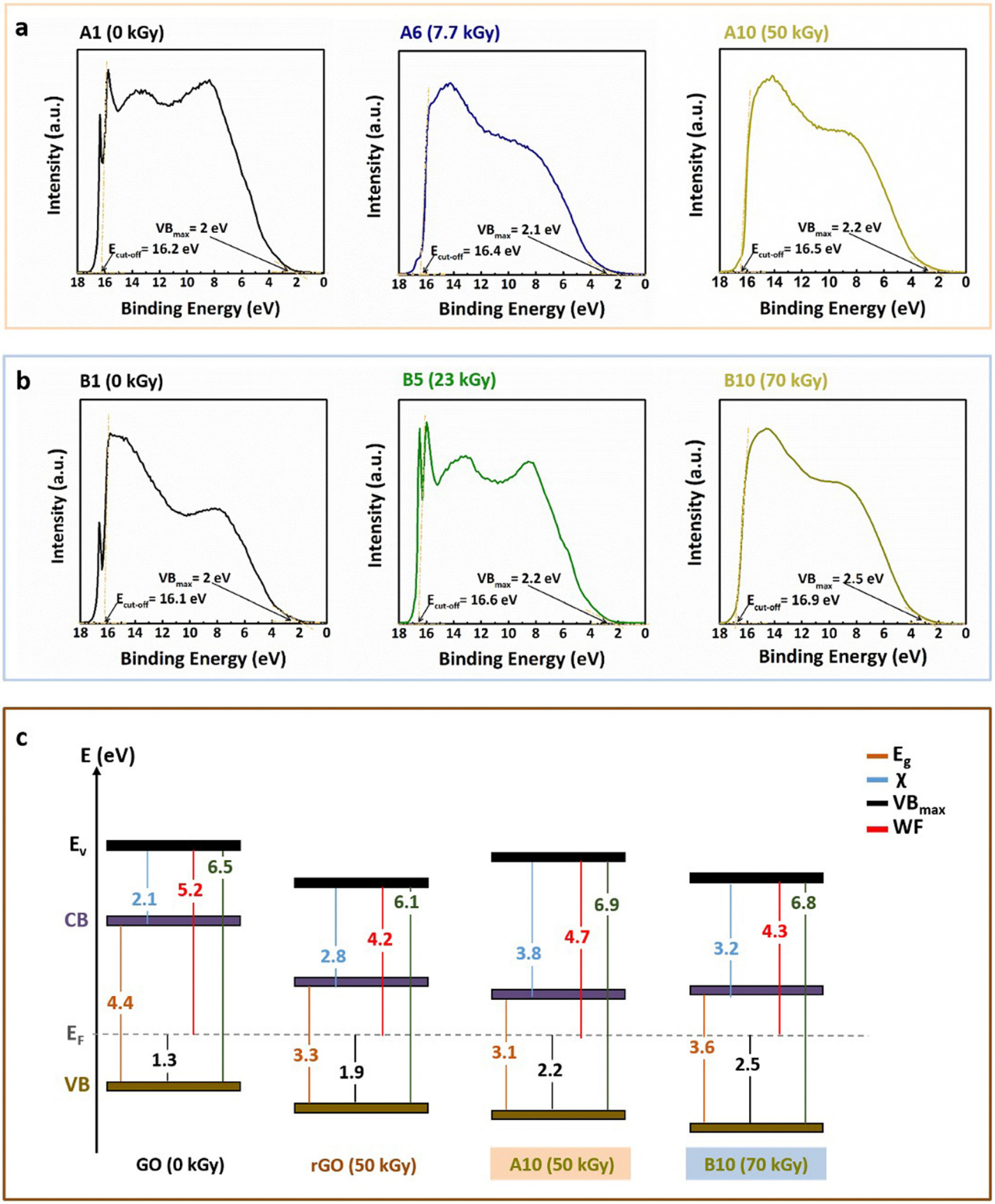

Fig. 3 Evolution of UPS spectra, obtained using HeI radiation ($h\nu$ = 21.21 eV) for rGO–Ag NPs composites at varying absorbed doses: (a) series A ($[Ag^+]_0 = 10^{-3}$ mol L^{-1}, A1 (0 kGy), A6 (7.7 kGy), A10 (50 kGy)), (b) series B ($[Ag^+]_0 = 10^{-2}$ mol L^{-1}, B1 (0 kGy), B5 (23 kGy), B10 (70 kGy)). (c) Band diagrams illustrating changes in the electronic structure: GO before irradiation, rGO synthesized with 50 kGy irradiation without silver ions, and rGO–Ag NPs synthesized at 50 kGy ($[Ag^+]_0 = 10^{-3}$ mol L^{-1}, sample A10 (50 kGy)) and 70 kGy ($[Ag^+]_0 = 10^{-2}$ mol L^{-1}, sample B10 (70 kGy)).

ions has a minimal effect on the final electronic properties of the rGO–Ag NPs composites when irradiated at high doses. On the other hand, the work function values for rGO before irradiation were observed to be slightly lower (1.9 eV for VB_{max} and 17 eV for $E_{cut\text{-}off}$).

To complete this UPS study, the positions of the VB and CB of the radiosynthesized materials relative to the E_F, as well as the WF of each sample, were determined using the same calculation methods detailed in Section 2.6. Tables 1 and 2 summarize the values obtained for each sample. Fig. S5 and S6 (ESI†) also illustrate the evolution of the band structure of our radiosynthesized rGO–Ag NPs composites.

For series A (Table 1), the absorbed dose resulted in a decrease in the bandgap from 4.4 eV to 3.1 eV, with a simultaneous increase in VB_{max} (from 2.0 eV to 2.2 eV) and $E_{cut\text{-}off}$ (from 16.2 eV to 16.5 eV). The work function also decreased from 5.0 eV to 4.7 eV, suggesting that the modification in the work function is related to the changes in the band structure caused by irradiation. The CB increased from 2.6 eV to 3.8 eV, reflecting a shift towards a more reduced state of the rGO–Ag NPs composites. This is illustrated in Fig. S5 (ESI†).

For series B (Table 2), the bandgap (E_g) also decreased from 5.0 eV to 3.6 eV, while VB_{max} increased from 2.0 eV to 2.5 eV. $E_{cut\text{-}off}$ increased from 16.1 eV to 16.9 eV, and the work function decreased from 5.1 eV to 4.3 eV with the absorbed dose. Similarly, to series A, the CB value of series B increased from 2.1 eV to 3.2 eV. This is illustrated in Fig. S6 (ESI†). This consistent trend across both series indicates that the absorbed dose is a key factor in modulating the electronic structure of the rGO–Ag NPs composites.

The evolution of all the energy values is consistent for both series, independent of the initial concentration of Ag^+ ions. However, the energy values before and after irradiation differ significantly, depending on silver ion concentration (0, 10^{-3}, or 10^{-2} mol L^{-1}). These data are summarized in Table 3. For comparison, the energy diagrams of GO before irradiation and rGO synthesized by radiolysis at 50 kGy without Ag^+ and with Ag^+ are presented in Fig. 3(c). These findings open up possibilities for further tailoring of the electronic structure of these materials through controlled irradiation and ion concentration, which could be beneficial for applications in catalysis, sensing, and other areas involving electronic interfaces.

3.4 XPS analysis

As previously demonstrated, the presence of Ag NPs, along with variations in Ag^+ concentration, significantly impacts the optical and electronic properties of radiolytically synthesized rGO composites. To further investigate the surface chemistry of these materials, XPS analysis was conducted on both irradiated and non-irradiated samples from series A and B, prepared with Ag^+ concentrations of 10^{-3} mol L^{-1} and 10^{-2} mol L^{-1}, respectively. This technique provides valuable insights into the surface-level chemical transformations, which are essential for understanding the reduction processes and the structural modifications occurring within the material.

The survey spectra of selected samples from series A and B are presented in Fig. 4(a) and (b), respectively. These spectra clearly indicate the presence of silver in the form of $AgClO_4$, alongside carbon and oxygen components derived from the GO structure, aligning with previous findings in the literature.[99–101] A significant observation is the increased silver content in series B, which was prepared with a higher Ag^+ concentration (10^{-2} mol L^{-1}). This highlights the critical role that Ag^+ concentration plays in determining the surface composition of the composites. The elevated silver content in series B is expected to influence both the reduction behavior and the electronic properties of the rGO–Ag NPs composite, as the increased Ag^+ concentration likely promotes greater interaction between silver ions and the rGO surface during the radiolytic reduction process. As absorbed dose increases, a clear reduction in the oxygen content (as indicated by the O1s band) was observed in both series (Fig. 4(a) and (b)). This deoxygenation process is attributed to the reduction of oxygenated groups on the surface, suggesting that irradiation induces the removal of oxygen functionalities. The reduction of oxygen groups is essential for the modification of material's electronic properties, as it leads to enhanced conjugation and conductivity of the rGO structure.

To investigate the reduction of Ag^+ to metallic Ag, the Ag 3d region of the XPS spectra was deconvoluted (Fig. 4(c) and (d)). The spectra show a prominent peak at 368.4 eV (Ag $3d_{5/2}$), which is characteristic of Ag^+ ions, and a peak at 369.6 eV corresponding to metallic silver (Ag^0 in its reduced state).[101] This indicates that irradiation effectively reduces Ag^+ into Ag^0 through radiolysis. Furthermore, at higher absorbed doses, the Ag $3d_{5/2}$ peak becomes slightly asymmetric, suggesting a minor degree of oxidation on the silver surface, likely due to the presence of residual oxygen in the system.

The C1s region of the XPS spectra for series A (samples A1 (0 kGy), A6 (7.7 kGy), and A10 (50 kGy)) and series B (samples B1 (0 kGy), B5 (23 kGy), and B10 (70 kGy)) are presented in Fig. 4(e) and (f), respectively. These spectra provide critical insights into the reduction of GO and the structural transformations occurring during irradiation. Two primary peaks are evident in the spectra: one at 284.6 eV, corresponding to sp^2 C═C bonds, and another at 285.1 eV, associated with sp^3 C–C bonds.[102–104] With increasing absorbed dose, a shift from sp^3 to sp^2 hybridization was observed, indicating an enhancement in the conjugation within the material. This shift is crucial for improving the electronic properties of the rGO–Ag NPs composites, as sp^2 carbon–carbon bonds are more conductive than sp^3 bonds. The decrease in sp^3 carbon content and the increase in sp^2 content with irradiation reflect the significant structural transformation induced by the irradiation process.[32]

In addition to the primary sp^2 and sp^3 peaks, minor components at higher binding energies (286 eV, 288 eV, and 289 eV) were attributed to carbon–oxygen bonds, such as C–O, C═O, and O–C═O groups. These components are indicative of oxygenated functionalities on the surface of rGO. With increasing absorbed doses, the intensity of these peaks decreases, providing further evidence of the reduction of oxygenated

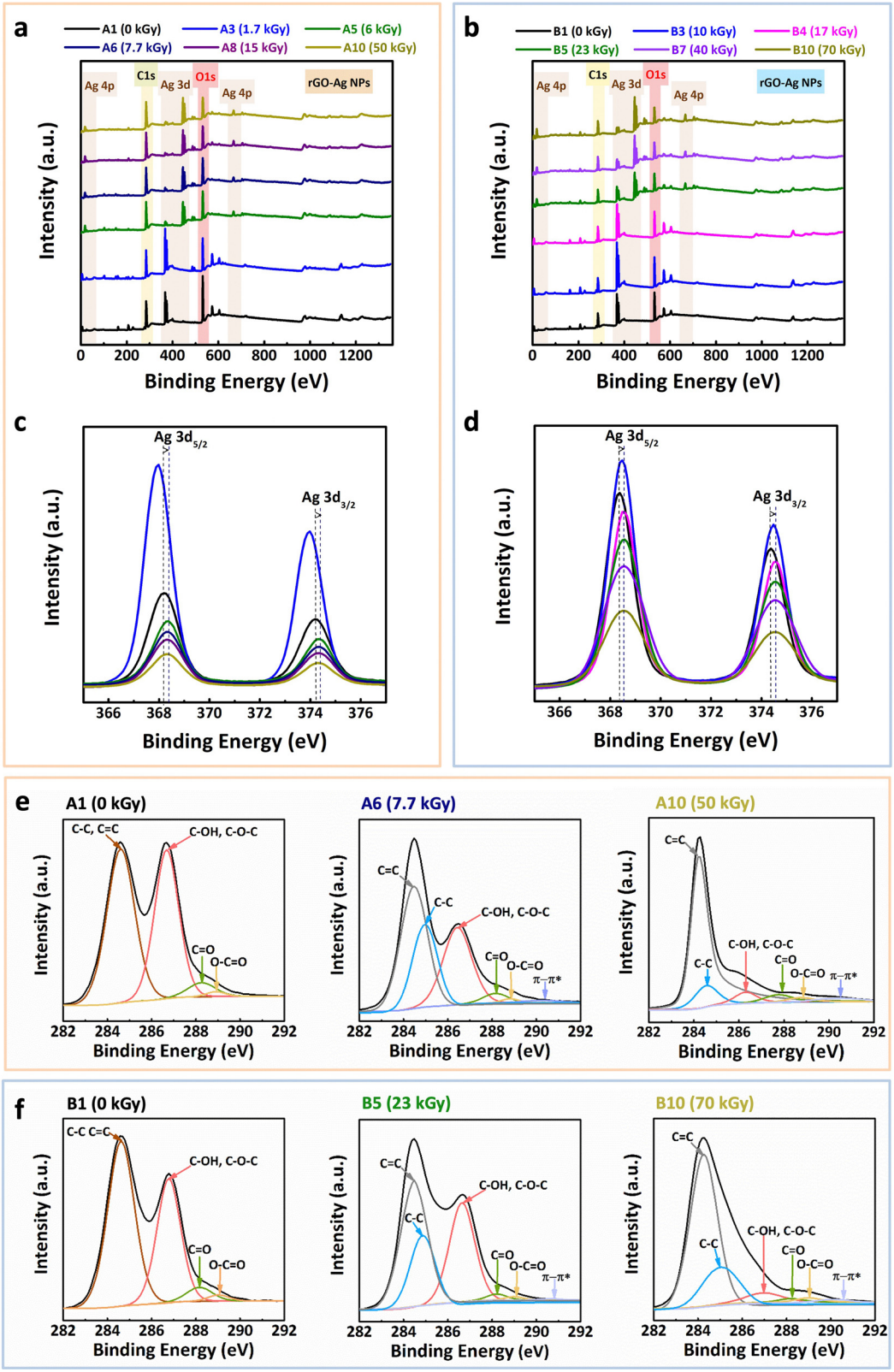

Fig. 4 XPS survey spectra showing the elemental composition of rGO–Ag NPs composites: (a) series A ([OG] = 0.2 g L^{-1}, [IPA] = 0.2 mol L^{-1}, [Ag^+] = 10^{-3} mol L^{-1}) and (b) series B ([OG] = 0.2 g L^{-1}, [IPA] = 0.2 mol L^{-1}, [Ag^+] = 10^{-2} mol L^{-1}). High-resolution XPS Ag 3d spectra highlighting the chemical states of silver: (c) series A and (d) series B. XPS C1s core-level spectra showing the evolution of carbon chemical states at varying absorbed doses: (e) series A (A1: 0 kGy, A6: 7.7 kGy, A10: 50 kGy) and (f) series B (B1: 0 kGy, B5: 23 kGy, B10: 70 kGy).

carbon species. This deoxygenation supports the hypothesis that irradiation facilitates the conversion of oxygenated carbon species into conjugated carbon–carbon bonds, enhancing the electronic conductivity of the material.

This XPS analysis confirms that irradiation facilitates both the reduction of Ag^+ to metallic Ag and the deoxygenation of GO, resulting in a more conjugated structure in rGO. The ability to control these surface chemical properties through irradiation presents a valuable approach to tailoring the characteristics of rGO–Ag NPS composites for electronic applications.

3.5 ATR-FTIR spectroscopy analysis

Building on the findings from XPS, which provided surface-level chemical information, ATR-FTIR spectroscopy offers complementary insights into the bulk chemical transformations of rGO–Ag NPs nanocomposites. This technique enables the detailed analysis of functional groups across the material's volume. ATR-FTIR spectra were recorded for both series A and B before and after irradiation to examine the effect of absorbed dose on the composition and stability of oxygen-containing functional groups within the composites. The obtained spectra are presented in Fig. 5(a) and (b).

For the non-irradiated samples (A1 and B1, 0 kGy), the FTIR spectra (black curves in Fig. 5(a) and (b)) exhibit distinct peaks characteristic of graphene oxide (GO). These include broad hydroxyl (–OH) stretching bands at 3450 cm^{-1}, ketone (C═O) vibrations at 1735 cm^{-1}, alkene (C═C) stretching at 1615 cm^{-1}, epoxide and C–O–C groups at 1230 cm^{-1}, and carboxylic acid C–O stretching at 1041 cm^{-1}. Additionally, the broad band between 3700–3100 cm^{-1} corresponds to water (H–OH) molecules associated with the hygroscopic nature of GO.[105,106] These peaks confirm the presence of oxygen-rich functional groups typical of GO in both series A and B.

Upon irradiation, significant changes are observed in the spectra of series A (Fig. 5(a)). A progressive reduction in the intensity of the bands characteristic of oxygen-containing functional groups, occurs with increasing dose, becoming especially notable up to 7.7 kGy (sample A6). At this absorbed dose, minimal oxygenated functional groups remain, as evidenced by the near disappearance of their associated bands.

Beyond 7.7 kGy, the spectra stabilize, indicating that further irradiation does not significantly alter the functional group composition. Concurrently, a band at 1590 cm^{-1}, attributed to C═C stretching in aromatic rings, becomes prominent, signifying the partial restoration of the conjugated aromatic network characteristic of rGO. This result aligns with literature findings and previous work, suggesting a significant restructuring of the composite's conjugated network during irradiation.[32,107–109]

In contrast, the spectra for series B (Fig. 5(b)) reveal a similar but less pronounced trend. Although the intensity of oxygen-containing functional group bands decreases with increasing absorbed dose, residual oxygenated functional groups persist even at the highest dose of 70 kGy (sample B10). This aligns with the XPS results, which also show incomplete deoxygenation for series B at higher doses. The persistence of these groups is likely due to the higher Ag^+ concentration in series B, which may modulate the radiolytic reduction process and limit complete deoxygenation.

Overall, ATR-FTIR analysis confirms the restoration of the conjugated sp^2 carbon network in rGO upon radiolytic reduction of GO, with the elimination of most oxygen-containing functional groups in both series A and B. The differences between the two series underscore the influence of Ag^+ concentration on the extent of deoxygenation and aromatic network restoration. These findings enhance the understanding of how irradiation parameters and silver ion

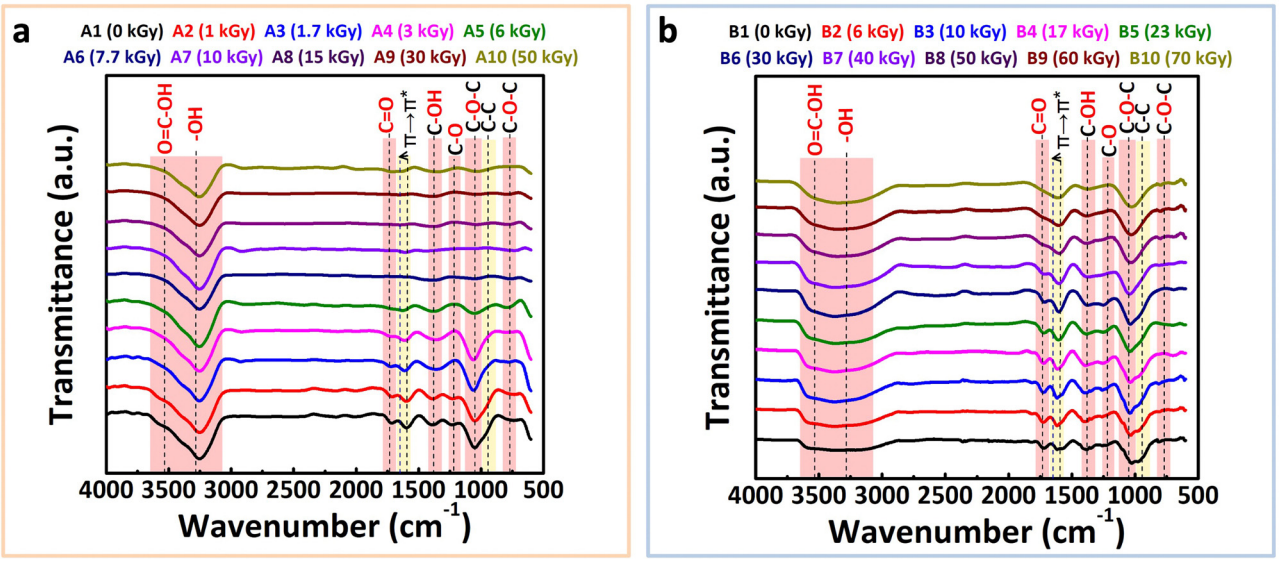

Fig. 5 ATR-FTIR spectra of non-irradiated and irradiated OG (0.2 g L^{-1})–Ag^+ at increasing absorbed doses (under N_2): (a) $[Ag^+] = 10^{-3}$ mol L^{-1} (series A) and (b) $[Ag^+] = 10^{-2}$ mol L^{-1} (series B).

concentration affect the structural and chemical evolution of rGO–Ag NPs nanocomposites.

3.6 Raman spectroscopy analysis

Following the ATR-FTIR analysis, which offered insight into the chemical structure of the rGO–Ag NPs nanocomposites, Raman spectroscopy was used to evaluate their structural properties and assess changes induced by irradiation.

Raman spectra, shown in Fig. 6(a) and (b) for series A and B, highlight characteristic rGO bands: D, G, 2D, and D + D′, located at 1350 cm^{-1}, 1580 cm^{-1}, 2700 cm^{-1}, and 2950 cm^{-1}, respectively. These features confirm the presence of rGO in the nanocomposites, which is consistent with prior analyses and literature findings for rGO alone.[32,110]

A key observation in this study is the enhanced intensity of the Raman signal for samples containing silver nanoparticles, a phenomenon that can be attributed to surface-enhanced Raman scattering (SERS) effects.[111] The increase in signal intensity is proportional to the concentration of silver in the composite, as evidenced by the more prominent bands in series B compared to those of series A. This intensity enhancement confirms that the silver nanoparticles effectively contribute to the SERS effect by amplifying the Raman response, a result of localized surface plasmon resonance associated with nanoscale silver.

The intensity ratio (I_D/I_G) between D and G bands, often used to quantify the degree of disorder in carbon-based materials, was analyzed for each series to assess structural variations with irradiation. In series A (Fig. 6(c)), the I_D/I_G ratio rises from 0.99 before irradiation to 1.18 at 50 kGy, suggesting an increase in defect density likely due to the formation of new sp^2 domains. A similar trend is seen in series B (Fig. 6(d)), where I_D/I_G also increases from 1.00 to 1.18, in agreement with values typically observed for rGO–Ag nanocomposites. Interestingly,

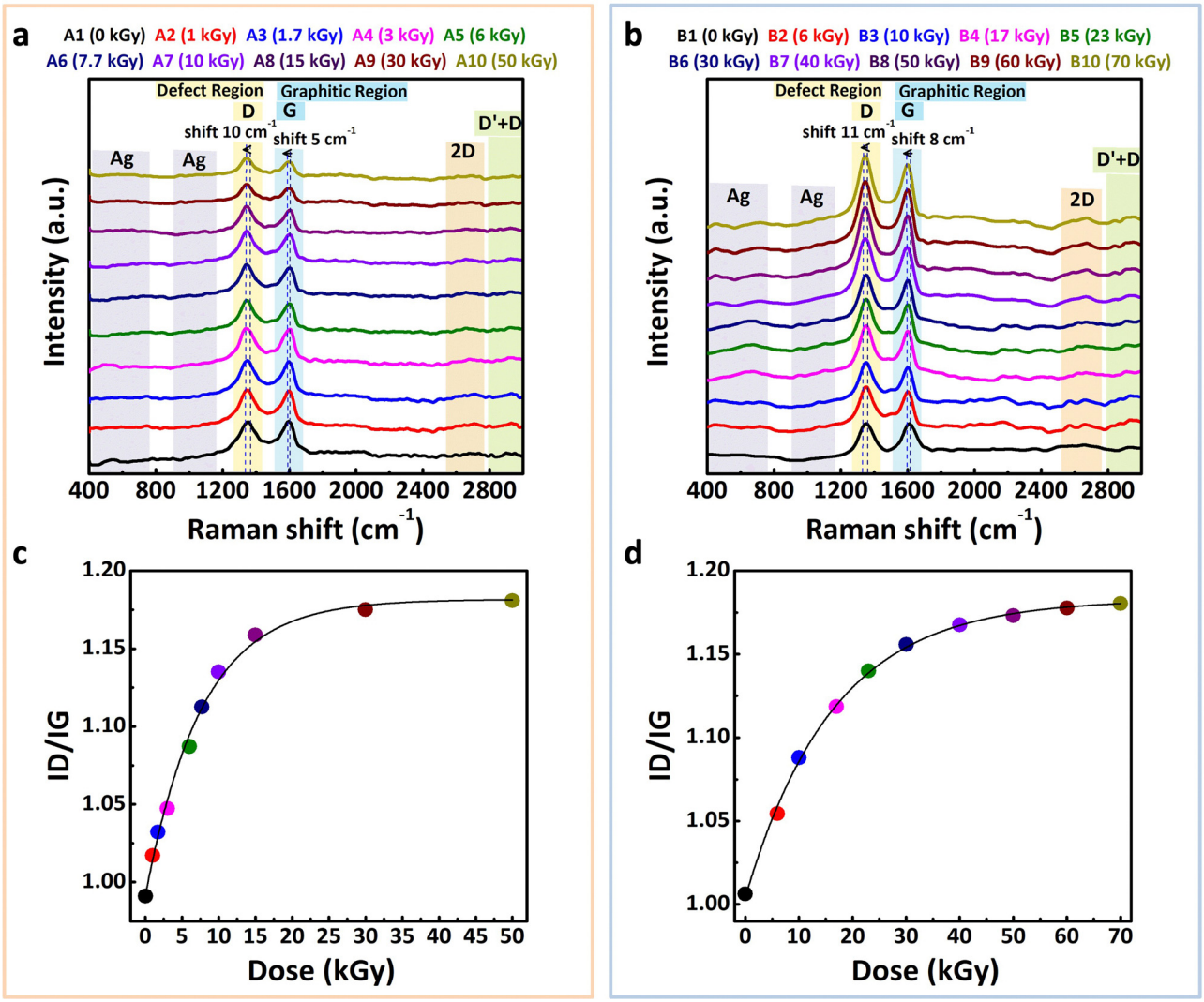

Fig. 6 Raman spectra of non-irradiated and irradiated OG (0.2 g L^{-1})–Ag^+ samples at increasing absorbed doses, taken with a 1 mW laser: (a) series A, (b) series B. Exponential fitting of the I_D/I_G ratio as a function of the absorbed dose: (c) series A, (d) series B. The uncertainty associated with the obtained values is less than 5%.

this ratio is lower than that observed for pure rGO (1.40),[32] indicating that the presence of silver contributes to a reduction in structural defects, possibly due to stabilization of the rGO structure.

These results highlight the crucial role of silver in enhancing Raman sensitivity and reducing defect density within the rGO–Ag NPs nanocomposites. Furthermore, they underscore the effectiveness of the radiolytic synthesis method in fabricating stable nanocomposites with optimized structural and spectroscopic characteristics, consistent with findings reported in the literature.[112–114]

3.7 SEM and EDX combined analysis

To further confirm the successful one-pot radiolytic synthesis of rGO–Ag nanocomposites, the morphological and compositional evolution of both series A and B samples was analyzed in detail by using scanning electron microscopy coupled with energy-dispersive X-ray spectroscopy. This analysis elucidates the morphological evolution of graphene oxide sheets and the spatial distribution of silver nanoparticles under varying gamma-irradiation dose. To remember, the samples contained consistent concentrations of GO (0.2 g L^{-1}) and IPA (0.2 mol L^{-1}), with two distinct initial silver ion concentrations: 10^{-3} mol L^{-1} (series A) and 10^{-2} mol L^{-1} (series B), ensuring controlled comparisons between the two systems.

The SEM images of selected samples, as presented in Fig. 7(a) and (b), provide a visual representation of the microstructural changes as a function of absorbed dose for series A and series B, respectively.

In the unirradiated samples A1 (0 kGy) and B1 (0 kGy), the morphology of GO remains unchanged, with large flat graphene oxide sheets clearly visible. Notably, no silver nanoparticles were observed in these samples, indicating that in the absence of light, under aluminium, Ag^+ ions were not reduced onto GO sheets prior to irradiation.

Upon gamma-irradiation, a notable morphological transformation occurs in both series. In series A (Fig. 7(a)), the initial absorbed doses lead to the formation of spherical Ag NPs that begin to decorate the GO sheets. These nanoparticles are relatively uniform in size and are evenly distributed across the surface of the sheets. The average diameter of AgNPs in this series was measured to be approximately 42 nm at an initial concentration of 10^{-3} mol L^{-1}. This rapid formation of silver nanoparticles indicates the efficient reduction of Ag^+ ions, which is consistent with the 1.7 kGy required to reduce silver ions at an initial concentration of 10^{-3} mol L^{-1}. Up to a dose of 7.7 kGy, which corresponds to the complete reduction of both GO and Ag^+ ions in series A, the graphene sheets remain smooth and planar. However, as the absorbed dose reaches 7.7 kGy, a noticeable transformation occurs in the structure of the GO sheets when their reduction into rGO is theoretically complete. This transformation is accompanied by the curvature of the GO sheets, interlayer entanglement, and the onset of sheet aggregation, typical of rGO. This could be explained by the radiation-induced drastic consumption of oxygenated functionalities which induces the enhancement of hydrophobic interactions within rGO sheets and between different rGO sheets. Despite these structural changes, the size and distribution of the Ag NPs remain stable across all doses, which underscores the robustness of the nanocomposites synthesized through this radiolytic process. This stability of silver nanoparticles, even at higher absorbed doses, suggests that the reduction of Ag^+ does not result in nanoparticle aggregation or changes in particle size, ensuring the consistency of the nanocomposite's structure and properties.

For series B (Fig. 7(b)), the higher initial concentration in Ag^+ ions (10^{-2} mol L^{-1}) led to a higher density of Ag NPs upon irradiation. The average diameter for this series was measured to be approximately 60 nm. A progressive increase in the number of Ag NPs is observed as the absorbed dose increases, with a notable increase in nanoparticle density up to a dose of 17 kGy, which corresponds to the complete reduction of Ag^+ ions. The Ag NPs in series B are slightly larger than those in series A, which is consistent with the broader and red-shifted plasmon absorption bands observed in UV-Vis absorption spectra (Fig. 2(b) *versus* Fig. 2(a)). This red-shift reflects the changes in particle distribution and optical properties as the nanoparticles grow in size. Despite the increased nanoparticle size at doses up to 17 kGy, no further size increase is observed upon subsequent irradiation. Once the silver reduction process reaches completion at 17 kGy, the distribution of Ag NPs across the graphene sheets stabilizes and no further aggregation is observed.

At this stage, after the complete reduction of Ag^+ ions, the reduction of GO begins. Up to an absorbed dose of 23 kGy, which corresponds to the complete reduction of both GO and Ag^+ ions in series B, the graphene sheets remain relatively smooth and planar. Above 23 kGy, one can observe morphological changes, including the formation of sheet curvature, folding, and eventual aggregation of rGO sheets, as described in case of series A after 7.7 kGy.

These morphological transformations align closely with the kinetic reduction processes previously discussed in Section 3.1, further confirming the interdependent reduction of silver ions and graphene oxide in the radiosynthesis of rGO–Ag NPs nanocomposites.

The EDX analysis (see Fig. S7, ESI†) complemented these observations by confirming the elemental composition of the nanocomposites. The detected elements include carbon, oxygen, silver, and chlorine, the latter originating from the silver perchlorate precursor used in the synthesis. Series B samples exhibit higher silver and chlorine concentrations due to their tenfold greater initial $AgClO_4$ content. Of particular interest in this study is the evolution of the carbon-to-oxygen (C/O) ratio, as it provides a clear indication of the degree of reduction of GO in both series. The C/O ratio, derived from EDX measurements, indeed serves as a reliable parameter to track the reduction process as a function of the absorbed dose.

Fig. 7(c) and (d) illustrate the evolution of the C/O ratio with absorbed dose for series A and series B, respectively. Initially, for the unirradiated samples (A1 and B1), the C/O ratios are both 3.0, which reflects the oxygen-rich nature of GO. As the

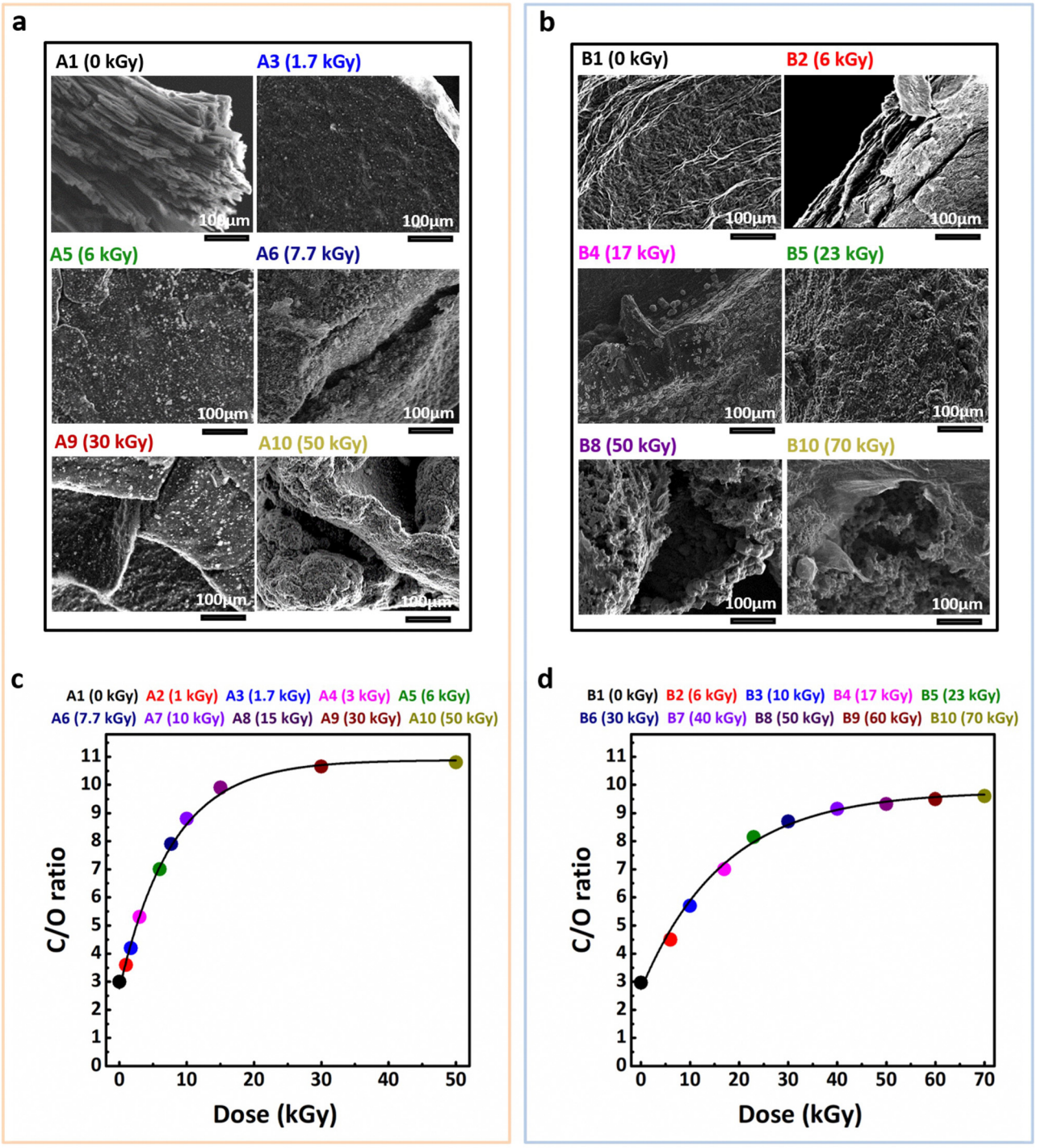

Fig. 7 (a) SEM images of series A samples: A1 (0 kGy), A3 (1.7 kGy), A6 (7.7 kGy), and A10 (50 kGy). (b) SEM images of series B samples: B1 (0 kGy), B4 (17 kGy), B5 (23 kGy), and B10 (70 kGy). Exponential fitting of the C/O ratio evolution with absorbed dose for rGO–Ag NPs composites: (c) series A ([GO] = 0.2 g L^{-1}, [IPA] = 0.2 mol L^{-1}, [Ag^+] = 10^{-3} mol L^{-1}) and (d) series B ([GO] = 0.2 g L^{-1}, [IPA] = 0.2 mol L^{-1}, [Ag^+] = 10^{-2} mol L^{-1}). The experimental uncertainty is less than 5%.

absorbed dose increases, the C/O ratio in series A gradually rises, reaching 10.8 at 50 kGy, indicating significant deoxygenation during rGO formation. Similarly, in series B, the C/O ratio reaches 9.6 at 70 kGy, reflecting a comparable degree of reduction, albeit with a slightly lower value due to the higher initial Ag^+ ion concentration in this series.

These findings are consistent with trends observed in XPS and ATR-FTIR spectra, reinforcing the deoxygenation process of GO under gamma-irradiation and aligning with findings reported in the literature.[115–118]

Notably, in previous studies where silver was absent,[32] the C/O ratio reached a slightly higher value of 11.2, which suggests

Table 4 Comparative study of C/O ratios for GO, rGO (50 kGy), and GO–Ag^+ at different silver ion concentrations before and after irradiation (A1, B1, A10, and B10)

Samples	C/O ratio
GO (0.2 g L^{-1}) (0 kGy)	3.1[32]
rGO (50 kGy)	11.2[32]
A1: GO (0.2 g L^{-1}) + Ag^+(10^{-3} mol L^{-1}) (0 kGy)	3.0
A10: rGO–Ag NPs (50 kGy)	10.8
B1: GO (0.2 g L^{-1}) + Ag^+(10^{-2} mol L^{-1}) (0 kGy)	3.1
B10: rGO–Ag NPs (70 kGy)	9.6

that the complete deoxygenation process is more pronounced in the absence of silver. This discrepancy highlights the role of silver concentration in modulating the reduction degree of GO.

The data presented in Table 4 underscores this observation, further emphasizing the impact of Ag^+ concentration on the efficiency of graphene oxide reduction in the synthesis of rGO–Ag nanocomposites.

3.8 TGA analysis

TGA analysis was further conducted to understand the role of silver nanoparticles in influencing the thermal behavior of rGO and to evaluate the thermal stability of the radiosynthesized rGO–Ag NPs nanocomposites. Fig. 8 presents the TGA profiles obtained under a nitrogen atmosphere for unirradiated GO, rGO synthesized at 50 kGy in the absence of silver ions (from a previous study), and the rGO–Ag NPs nanocomposites synthesized in presence of silver ions: A10 (50 kGy) from series A and B10 (70 kGy) from series B.

The TGA profile of GO reveals a characteristic three-stage thermal degradation process. In the first stage, around 100 °C, approximately 10% weight loss occurs, attributed to the evaporation of water molecules trapped within the hydrophilic GO structure. The second stage, beginning around 200 °C, shows a significant 27% weight loss associated with the decomposition of oxygenated functional groups such as hydroxyl, epoxy, and carbonyl groups. In the final stage, between 400 and 500 °C, a dramatic 51% weight loss is observed, corresponding to the degradation of the carbon backbone. This extensive weight loss reflects the structural instability of GO and aligns with previously reported thermal behavior for such materials.

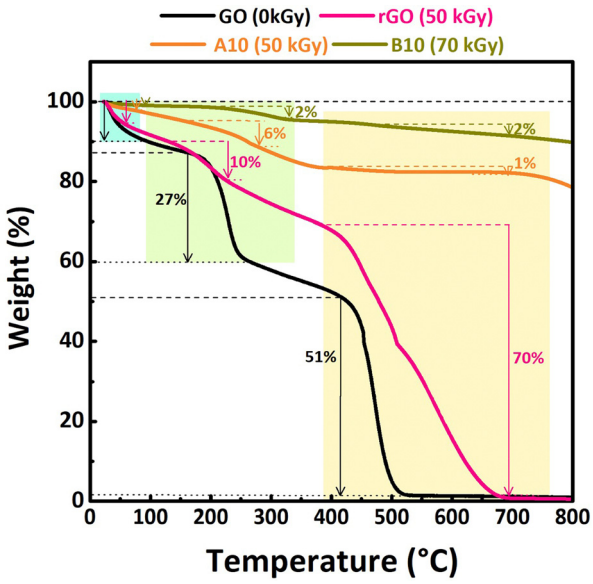

Fig. 8 TGA profiles obtained under nitrogen atmosphere for GO and rGO synthesized at 50 kGy in the absence of silver ions, and rGO–Ag NPs nanocomposites synthesized at 50 kGy (sample A10, series A) and at 70 kGy (sample B10, series B) in presence of silver ions.

In contrast, rGO synthesized *via* radiolytic reduction at 50 kGy demonstrates significantly enhanced thermal stability. The first two stages of degradation are notably reduced, with only a 10% weight loss occurring in the 160–280 °C range, attributed to the removal of most oxygenated functional groups during the reduction process. In the final stage, a 70% weight loss is observed between 400 and 700 °C. This shift to higher degradation temperatures indicates enhanced thermal stability of rGO compared to GO. The reduction process restores the sp^2 carbon network, which requires higher temperatures for decomposition due to its increased structural integrity. The greater weight loss at these higher temperatures reflects the complete degradation of the more stable carbon framework. While radiolytic reduction effectively removes oxygenated groups, any residual defects or weak points in the structure may still influence decomposition, but they do not negate the overall improved thermal resilience of rGO.

For the rGO–Ag NPs nanocomposites, both A10 (50 kGy) and B10 (70 kGy) exhibit markedly improved thermal stability compared to rGO alone. In the first stage, no significant weight loss is observed below 200 °C, indicating the effective removal of residual water. In the second stage, minor weight losses of 6% for A10 (50 kGy) and 2% for B10 (70 kGy) are attributed to the decomposition of residual oxygenated functional groups.[119] These reduced losses highlight the stabilizing effect of Ag NPs, which likely minimize the presence of thermally unstable groups. In the final stage (300–800 °C), weight loss remains low, with a maximum of approximately 20% for A10 (50 kGy) and just 10% for B10 (70 kGy). The superior stability of the nanocomposites is first attributed to the interaction between silver nanoparticles and the graphene sheets, which likely act as thermal barriers and restrict carbon framework decomposition at elevated temperatures, but it is also explained by the high silver content within rGO–Ag NPs composites. Among the composites, B10 (70 kGy), synthesized with a higher silver ion concentration (10^{-2} mol L^{-1}), shows the lowest overall weight loss in the TGA analysis. This is primarily due to its higher silver content, estimated to be about 90 wt%, compared to approximately 80 wt% for A10 (50 kGy). The apparent enhanced thermal stability is thus largely a result of the higher proportion of thermally stable silver nanoparticles rather than an intrinsic change in the rGO's thermal properties.[120] The uniform distribution of silver nanoparticles within the graphene matrix may contribute to the overall thermal behavior of the composites, potentially influencing the decomposition process of the carbonaceous component.

Interestingly, the gradual increase in silver content from series A to series B not only improves thermal stability but also aligns with the observed reduction trends in chemical composition, as evidenced by the increasing C/O ratio with absorbed dose. These observations are consistent with previously reported findings, where metal nanoparticle incorporation enhances the thermal properties of graphene derivatives, highlighting the reproducibility and robustness of the radiolytic approach. The findings suggest that optimizing the concentration of the silver precursor during synthesis could serve as a strategic approach to tailor the thermal properties of graphene-based nanocomposites for specific applications.

3.9 Cyclic voltammetry analysis

Following the exploration of the physicochemical, structural, and thermal stability properties of our samples (series A and B), the focus shifted to examining their electrochemical characteristics through cyclic voltammetry. CV is an essential tool for rapid and straightforward evaluation of surface properties and interactions of materials within a reaction medium. By applying a linearly varying potential, CV reveals critical insights into redox behavior and material's electron transfer capabilities, with the electrode surface playing a pivotal role as the site of electrochemical reactions. Here, the samples were characterized by CV in an aqueous 0.1 M KOH electrolyte at ambient temperature, within a potential range of −0.4 V to +0.4 V *vs.* Ag/AgCl. This approach aimed to analyze the oxidation and reduction reactions of silver and to compare the CV profiles of rGO–Ag NPs composites with that of rGO alone, in the absence of silver. Additionally, this study examined the evolution of specific capacitance as a function of absorbed dose and silver ion concentration to understand their effects on the material's electrochemical performances.

Fig. 9(a) and (b) show the cyclic voltammograms (CVs) for the nanocomposites from series A and B, respectively, covering both non-irradiated (A1 (0 kGy) and B1 (0 kGy)) and irradiated samples at different absorbed doses (A6 (7.7 kGy), A10 (50 kGy) in series A, and B5 (23 kGy), B10 (70 kGy) in series B) recorded at scan rates ranging from 10 to 200 mV s^{-1}. Additional CVs for all samples from series A and B are provided in Fig. S8 and S9 (ESI†), respectively. The CV results demonstrate a progressive increase in current density with scan rate for all samples in both series, indicating robust specific capacitance. These voltammograms reveal characteristic redox peaks, which reflect the faradaic processes occurring at the electrode surface. For series A (Fig. 9(a) and Fig. S8, ESI†), two primary domains are observed during the positive potential sweep: a broad double-layer region spanning −0.4 V to 0.2 V *vs.* Ag/AgCl and an oxidation peak around 0.34 V, followed by a reduction peak near 0.07 V. For series B (Fig. 9(b) and Fig. S9, ESI†), a similar pattern emerges with a broad double-layer region in the range of −0.4 V to 0.2 V *vs.* Ag/AgCl and two distinct oxidation peaks at 0.26 V and 0.34 V, respectively. Notably, the oxidation peaks in the positive potential sweep appear more pronounced with increased silver concentration, whereas the reduction process features a single peak with a maximum at approximately 0.05 V *vs.* Ag/AgCl. An increase in both anodic and cathodic currents with increasing Ag concentration is evident, reflecting enhanced capacitive behavior.

A comparative analysis of the irradiated and non-irradiated samples shows a substantial increase in the area under the charge and discharge curves with rising absorbed dose, suggesting an enhancement in specific capacitance as a function of absorbed dose. The observed broad double-layer in both series can be attributed to the pseudo-capacitive contributions from the rGO matrix (manifested by the quasi-rectangular shape) as well as the minor metallic behavior of the Ag NPs. This minor metallicity of Ag NPs was corroborated through UV-Vis absorption spectroscopy, which exhibited broad plasmon absorption peaks, indicating non-metallic characteristics.

To further elucidate the impact of absorbed dose and Ag concentration on electrochemical performance, specific capacitances were calculated for each sample from the CV curves obtained at different scan rates (10 to 200 mV s^{-1}) using a three-electrode configuration. Fig. 9(c) and (d) display the evolution of specific capacitance as a function of scan rate for all samples in series A and B, respectively. At higher scan rates (40 to 200 mV s^{-1}), specific capacitance tends to decrease linearly for all samples, highlighting the influence of ion mobility limitations. At lower scan rates (<40 mV s^{-1}), the specific capacitance decreases more sharply, potentially due to contributions from porosity.[121,122]

Specific capacitance values calculated at 10 mV s^{-1} across various absorbed doses are presented in Fig. 9(e) and (f). For series A composites synthesized with 10^{-3} mol L^{-1} Ag^+ (Fig. 9(e)), specific capacitance increased from 46.5 F g^{-1} (before irradiation) to 218.0 F g^{-1} (post-irradiation at 50 kGy). Similarly, for series B composites synthesized with 10^{-2} mol L^{-1} Ag^+ (Fig. 9(f)), specific capacitance rose from 63.0 F g^{-1} (before irradiation) to 298.0 F g^{-1} (post-irradiation at 70 kGy). This trend demonstrates a notable enhancement in specific capacitance attributable to both irradiation and increased Ag^+ concentration. In comparison, rGO synthesized at 50 kGy in the absence of silver ions, exhibited a maximum specific capacitance of 125.4 F g^{-1} at 10 mV s^{-1} in 0.1 M KOH electrolyte. Table 5 summarizes the specific capacitance values obtained at 10 mV s^{-1} for all radio-synthesized samples, with and without silver. These findings clearly reveal the beneficial impact of Ag NPs on the capacitive response of the irradiated nanocomposites, where the specific capacitance increased by approximately 50% with a rise in Ag^+ concentration from 10^{-3} mol L^{-1} (series A) to 10^{-2} mol L^{-1} (series B). Furthermore, comparisons with the literature indicate that the specific capacitances of radiosynthesized rGO–Ag NPs composites surpass those reported for similar materials, confirming the promising electrochemical properties of these nanocomposites.[123–125]

It should be noted that although KOH concentration in this study was fixed at 0.1 M, previous trials with rGO in 1 M KOH demonstrated an increase in specific capacitance up to 229.0 F g^{-1} at 100 mV s^{-1}, compared to 129.0 F g^{-1} with the 0.1 M KOH solution. These observations suggest that optimizing the KOH concentration in future studies could further

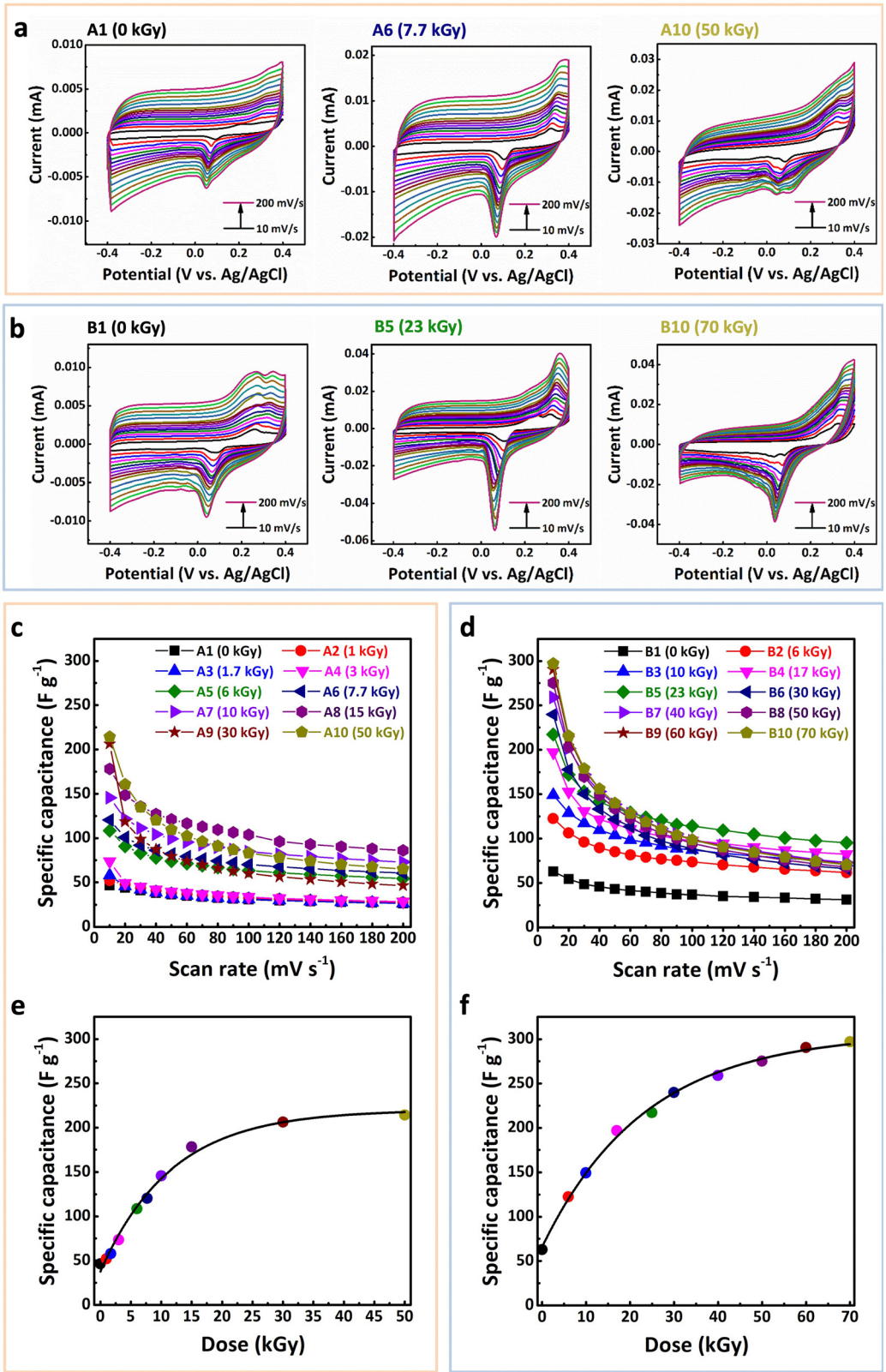

Fig. 9 Cyclic voltammograms of rGO–Ag NPs composites from (a) series A (A0, A6, A10) and (b) series B (B0, B5, B10), measured in 0.1 M KOH solution at ambient temperature. Voltammograms were recorded at scan rates between 10 and 200 mV s^{-1} over a potential range of −0.4 V to +0.4 V *vs.* Ag/AgCl. Specific capacitance of the composites measured at different scan rates (10–200 mV s^{-1}) for samples of (c) series A and (d) series B. Exponential curve fitting of the variation in specific capacitance with absorbed dose at 10 mV s^{-1} for (e) series A (e) and (f) series B.

Table 5 Comparative study of specific capacitance values for rGO before and after irradiation, with and without silver. The table presents the specific capacitance values measured in 0.1 M KOH solution at a scan rate of 10 mV s^{-1}, highlighting the effect of irradiation and silver addition on the capacitive performances of rGO

Samples	Specific capacitance ($F\ g^{-1}$) at 10 mV s^{-1}
GO (0.2 g L^{-1}) (0 kGy)	6.8
rGO (50 kGy)	125.4
A1: GO (0.2 g L^{-1}) + Ag^+(10^{-3} mol L^{-1}) (0 kGy)	46.5
A10: rGO–Ag NPs (50 kGy)	218.0
B1: GO (0.2 g L^{-1}) + Ag^+(10^{-2} mol L^{-1}) (0 kGy)	63.0
B10: rGO–Ag NPs (70 kGy)	298.0

enhance the specific capacitance of these rGO–Ag NPs composites, particularly in higher-concentration electrolyte conditions.

4. Conclusion

The present study has effectively demonstrated the potential of gamma-induced radiolysis as a powerful and versatile method for the one-pot synthesis of rGO–Ag NPs composites. By maintaining consistent concentrations of graphene oxide at 0.2 g L^{-1} and isopropanol at 0.2 mol L^{-1}, while varying the silver ion concentrations to 10^{-3} mol L^{-1} in series A and 10^{-2} mol L^{-1} in series B, precise control over the properties of the resulting nanocomposites was achieved. The systematic variation of absorbed doses, specifically 7.7 kGy for series A and 23 kGy for series B, confirmed the efficiency of the one-pot reduction process. Importantly, findings demonstrated that the reduction of silver ions occurs approximately seven times faster than that of graphene oxide in series A and about seventy times faster in series B.

The multi-technique characterization approach employed in this research work revealed several significant findings that underscore the effectiveness of this synthesis method. Analyses using UPS and UV-Vis spectroscopies showed a substantial reduction in band gap energy, decreasing from 4.4 eV to 3.1 eV for series A and from 5.0 eV to 3.6 eV for series B, indicating enhanced electronic properties of the synthesized nanocomposites. The data obtained from these techniques facilitated the construction of energy band diagrams for all samples in both series A and B, marking a significant advancement in the literature. This is the first time such detailed energy band diagrams have been presented for rGO–Ag nanocomposites synthesized through gamma-induced radiolysis or by other synthetic methods.

Structural transformations were confirmed through XPS and ATR FTIR spectroscopies, which indicated effective concomitant reduction of graphene oxide and silver ions, along with a notable shift from sp^3 to sp^2 hybridization in the carbon network that enhances conductivity. A comparative analysis between series A and B revealed that while both series exhibited improved electronic properties, series B demonstrated even greater enhancements due to the higher concentration of silver ions. The I_D/I_G ratio obtained from Raman spectroscopy decreased from 1.40 for pure graphene oxide to 1.18 for rGO–Ag nanocomposites, comparable to defect levels reported for composites synthesized by other methods, indicating minimal structural defects in the rGO matrix. Importantly, no significant structural defects were introduced into the rGO matrix regardless of whether silver was present at concentrations of 10^{-3} or 10^{-2} mol L^{-1}.

SEM characterization complemented these findings by providing visual confirmation of the uniform dispersion of silver nanoparticles on the rGO surface. EDX results further corroborated the successful incorporation of silver into the nanocomposites, confirming the elemental composition and distribution within the materials. Notably, the C/O ratio calculated from EDX significantly increased, with values of 10.8 and 9.6 for composites synthesized with 10^{-3} mol L^{-1} and 10^{-2} mol L^{-1} in silver, respectively, compared to 11.2 for rGO alone. These values are consistent with previously reported ratios for rGO nanocomposites, further validating the reduction process.

TGA analysis revealed enhanced thermal stability of rGO–Ag NPs composites compared to both pure graphene oxide and rGO alone. The composites exhibited minimal weight loss, with only 10% reduction observed between 300–800 °C. This falls within the range of thermal stability values reported for rGO–Ag composites synthesized by other methods, demonstrating the effectiveness of the radiolytic approach in producing thermally stable materials. This improved thermal behavior is primarily attributed to the presence of thermally stable silver nanoparticles, which contribute significantly to the overall thermal stability of the composite materials.

The electrochemical performance evaluated *via* cyclic voltammetry revealed remarkable specific capacitance values that reached up to 218 F g^{-1} at a scan rate of 10 mV s^{-1} for series A and an impressive 298 F g^{-1} for series B when tested in a 0.1 M KOH electrolyte, far exceeding the capacitance observed for rGO alone (125.4 F g^{-1}). Also, these values are consistent with or exceed the range of specific capacitances reported for chemically reduced rGO composites under similar conditions, showcasing the superior charge storage capabilities of the nanocomposites synthesized *via* radiolysis.

These findings underscore the advantages of the radiolytic synthesis method, which simplifies the production process while enabling precise control over material properties. The one-pot approach not only enhances the purity of the final product but also allows for scalability, making it a viable alternative to traditional synthesis methods that often rely on hazardous reducing agents. The remarkable properties exhibited by radiosynthesized nanocomposites open new avenues for applications across various fields. In energy storage, the high specific capacitance suggests potential use in supercapacitor electrodes. In catalysis, improved electronic properties and high surface area could enhance catalytic activity in chemical reactions. The unique optical characteristics may enable the development of highly sensitive sensors, while the incorporation of silver nanoparticles suggests potential applications in water treatment and antimicrobial solutions.

Author contributions

Souad Abou Zeid: methodology, formal analysis, investigation, conceptualization, software, validation, resources, writing – original draft, writing – review and editing, visualization. Liran Hu: formal analysis. Rasta Ghasemi: validation, investigation (SEM and EDX experiments). Matthieu Gervais: validation, investigation (TGA experiments). Jaspreet Kaur Randhawa: formal analysis, investigation (CV experiments). Prem Felix Siril: visualization, formal analysis, investigation (Raman experiments). Samy Remita: conceptualization, methodology, validation, writing – original draft, writing – review and editing, visualization, supervision, project administration.

Data availability

The data supporting this article have been included as part of the ESI.† Additional data will be made available on request.

Conflicts of interest

The authors declare that they have no known competing financial interests or personal relationships that could have appeared to influence the work reported in this paper.

Acknowledgements

The first author expresses profound gratitude to Dr Wafaa Noun of the Faculty of Science (Branch 1), Lebanese University, Lebanon, for her invaluable guidance, unwavering support, and insightful contributions that significantly enriched the course of this research. The authors also extend their sincere appreciation to the coordinators of the Franco-Indian SPARC (Scheme for Promotion of Academic and Research Collaboration) project no. P-32 for their generous support and collaborative efforts, which were instrumental in the successful execution of this work.

References

1 M. Rai, A. Yadav and A. Gade, Silver nanoparticles as a new generation of antimicrobials, *Biotechnol. Adv.*, 2009, **27**, 76–83.
2 X.-F. Zhang, Z.-G. Liu, W. Shen and S. Gurunathan, Silver Nanoparticles: Synthesis, Characterization, Properties, Applications, and Therapeutic Approaches, *Int. J. Mol. Sci.*, 2016, **17**, 1534.
3 K. M. F. Hasan, L. Xiaoyi, Z. Shaoqin, P. G. Horváth, M. Bak, L. Bejó, G. Sipos and T. Alpár, Functional silver nanoparticles synthesis from sustainable point of view: 2000 to 2023 – A review on game changing materials, *Heliyon*, 2022, **8**, e12322.
4 M.-C. Daniel and D. Astruc, Gold nanoparticles: assembly, supramolecular chemistry, quantum-size-related properties, and applications toward biology, catalysis, and nanotechnology, *Chem. Rev.*, 2004, **104**, 293–346.
5 M. C. Stensberg, Q. Wei, E. S. McLamore, D. M. Porterfield, A. Wei and M. S. Sepúlveda, Toxicological studies on silver nanoparticles: challenges and opportunities in assessment, monitoring and imaging, *Nanomedicine*, 2011, **6**, 879–898.
6 S. Guo and E. Wang, Noble metal nanomaterials: Controllable synthesis and application in fuel cells and analytical sensors, *Nano Today*, 2011, **6**, 240–264.
7 C. M. Cobley, J. Chen, E. C. Cho, L. V. Wang and Y. Xia, Gold nanostructures: a class of multifunctional materials for biomedical applications, *Chem. Soc. Rev.*, 2011, **40**, 44–56.
8 M. R. Jones, K. D. Osberg, R. J. Macfarlane, M. R. Langille and C. A. Mirkin, Templated Techniques for the Synthesis and Assembly of Plasmonic Nanostructures, *Chem. Rev.*, 2011, **111**, 3736–3827.
9 R. W. Murray, Nanoelectrochemistry: Metal Nanoparticles, Nanoelectrodes, and Nanopores, *Chem. Rev.*, 2008, **108**, 2688–2720.
10 Q. Li, J. Bian, J. Sun, J. Wang, Y. Luo, K. Sun and D. Yu, Controllable growth of well-aligned ZnO nanorod arrays by low-temperature wet chemical bath deposition method, *Appl. Surf. Sci.*, 2010, **256**, 1698–1702.
11 B. Li, C. F. Goh, X. Zhou, G. Lu, H. Tantang, Y. Chen, C. Xue, F. Y. C. Boey and H. Zhang, Patterning Colloidal Metal Nanoparticles for Controlled Growth of Carbon Nanotubes, *Adv. Mater.*, 2008, **20**, 4873–4878.
12 J. L. Fiorio, M. A. S. Garcia, M. L. Gothe, D. Galvan, P. C. Troise, C. A. Conte-Junior, P. Vidinha, P. H. C. Camargo and L. M. Rossi, Recent advances in the use of nitrogen-doped carbon materials for the design of noble metal catalysts, *Coord. Chem. Rev.*, 2023, **481**, 215053.
13 S. B. Malik, J. I. Saggu, A. Gul, B. A. Abbasi, J. Iqbal, S. Waris, Y. A. Bin Jardan and W. Chalgham, Synthesis and Characterization of Silver and Graphene Nanocomposites and Their Antimicrobial and Photocatalytic Potentials, *Molecules*, 2022, **27**, 5184.
14 Z. Hajjar, M. Kazemeini, A. Rashidi and S. Soltanali, Hydrodesulfurization catalysts based on carbon nanostructures: A review, *Fullerenes, Nanotubes Carbon Nanostruct.*, 2018, **26**, 557–569.
15 W. Wazir, Z. Ahmad, S. Zulfiqar, E. W. Cochran, S. Mubarik, T. Kousar, H. H. Somaily, J.-J. Shim, H. A. Alsalmah and M. Aadil, Synergistic effects of noble metal doping and nanoengineering on boosting the azo dye mineralization activity of nickel oxide, *Ceram. Int.*, 2023, **49**, 38026–38035.
16 T. A. Amollo, Metallic nanoparticles and hybrids of metallic nanoparticles/graphene nanomaterials for enhanced photon harvesting and charge transport in polymer and dye sensitized solar cells, *Heliyon*, 2024, **10**, e26401.
17 A. K. Geim, Graphene: status and prospects, *Science*, 2009, **324**, 1530–1534.
18 A. K. Geim and K. S. Novoselov, The rise of graphene, *Nat. Mater.*, 2007, **6**, 183–191.
19 D. G. Papageorgiou, I. A. Kinloch and R. J. Young, Mechanical properties of graphene and graphene-based nanocomposites, *Prog. Mater. Sci.*, 2017, **90**, 75–127.

20 M. J. McAllister, J.-L. Li, D. H. Adamson, H. C. Schniepp, A. A. Abdala, J. Liu, M. Herrera-Alonso, D. L. Milius, R. Car, R. K. Prud'homme and I. A. Aksay, Single Sheet Functionalized Graphene by Oxidation and Thermal Expansion of Graphite, *Chem. Mater.*, 2007, **19**, 4396–4404.
21 M. Czerniak-Reczulska, A. Niedzielska and A. Jędrzejczak, Graphene as a Material for Solar Cells Applications, *Adv. Mater. Sci.*, 2015, **15**, 67–81.
22 J. Zhu, R. Duan, S. Zhang, N. Jiang, Y. Zhang and J. Zhu, *J. Korean Phys. Soc.*, 2014, **3**, 1–8.
23 V. H. Luan, H. N. Tien, L. T. Hoa, N. T. M. Hien, E.-S. Oh, J. Chung, E. J. Kim, W. M. Choi, B.-S. Kong and S. H. Hur, Synthesis of a highly conductive and large surface area graphene oxide hydrogel and its use in a supercapacitor, *J. Mater. Chem. A*, 2013, **1**, 208–211.
24 X.-Y. Yan, X.-L. Tong, Y.-F. Zhang, X.-D. Han, Y.-Y. Wang, G.-Q. Jin, Y. Qin and X.-Y. Guo, Cuprous oxide nanoparticles dispersed on reduced graphene oxide as an efficient electrocatalyst for oxygen reduction reaction, *Chem. Commun.*, 2012, **48**, 1892–1894.
25 K. R. Amin and A. Bid, High-Performance Sensors Based on Resistance Fluctuations of Single-Layer-Graphene Transistors, *ACS Appl. Mater. Interfaces*, 2015, **7**, 19825–19830.
26 H. Huang, S. Su, N. Wu, H. Wan, S. Wan, H. Bi and L. Sun, Graphene-Based Sensors for Human Health Monitoring, *Front. Chem.*, 2019, **7**, 2296–2646.
27 T. Kuila, A. K. Mishra, P. Khanra, N. H. Kim and J. H. Lee, Recent advances in the efficient reduction of graphene oxide and its application as energy storage electrode materials, *Nanoscale*, 2013, **5**, 52–71.
28 A. T. Smith, A. M. LaChance, S. Zeng, B. Liu and L. Sun, Synthesis, properties, and applications of graphene oxide/reduced graphene oxide and their nanocomposites, *Nano Mater. Sci.*, 2019, **1**, 31–47.
29 D. Li, M. B. Müller, S. Gilje, R. B. Kaner and G. G. Wallace, Processable aqueous dispersions of graphene nanosheets, *Nat. Nanotechnol.*, 2008, **3**, 101–105.
30 S. Pei and H.-M. Cheng, The reduction of graphene oxide, *Carbon*, 2012, **50**, 3210–3228.
31 V. Agarwal and P. B. Zetterlund, Strategies for reduction of graphene oxide – A comprehensive review, *Chem. Eng. J.*, 2021, **405**, 127018.
32 S. Abou Zeid, S. Bencherif, R. Ghasemi, R. Gogoi, Y. Chouli, M. Gervais, D. Dragoe, J. Ghilane, P. F. Siril and S. Remita, Radiation induced reduction of graphene oxide: a dose effect study, *New J. Chem.*, 2024, **48**, 4749–4764.
33 Y. Zhu, S. Murali, W. Cai, X. Li, J. W. Suk, J. R. Potts and R. S. Ruoff, Graphene and graphene oxide: synthesis, properties, and applications, *Adv. Mater.*, 2010, **22**, 3906–3924.
34 F. Parnianchi, M. Nazari, J. Maleki and M. Mohebi, Combination of graphene and graphene oxide with metal and metal oxide nanoparticles in fabrication of electrochemical enzymatic biosensors, *Int. Nano Lett.*, 2018, **8**, 229–239.
35 S. W. Chook, C. H. Chia, S. Zakaria, M. K. Ayob, K. L. Chee, N. M. Huang, H. M. Neoh, H. N. Lim, R. Jamal and R. Rahman, Antibacterial performance of Ag nanoparticles and AgGO nanocomposites prepared *via* rapid microwave-assisted synthesis method, *Nanoscale Res. Lett.*, 2012, **7**, 541.
36 R. Pasricha, S. Gupta and A. K. Srivastava, A facile and novel synthesis of Ag-graphene-based nanocomposites, *Small*, 2009, **5**, 2253–2259.
37 Z. Zhang, F. Xu, W. Yang, M. Guo, X. Wang, B. Zhang and J. Tang, A facile one-pot method to high-quality Ag-graphene composite nanosheets for efficient surface-enhanced Raman scattering, *Chem. Commun.*, 2011, **47**, 6440–6442.
38 T. K. Das, S. K. Ghosh and N. C. Das, Green synthesis of a reduced graphene oxide/silver nanoparticles-based catalyst for degradation of a wide range of organic pollutants, *Nano-Struct. Nano-Objects*, 2023, **34**, 100960.
39 Y. Qian, C. Zhou, J. Zhou and A. Huang, Synthesis of silver-nanoparticles composite with highly catalytic activity supported on the reduced graphene oxide, *Appl. Surf. Sci.*, 2020, **525**, 146597.
40 Y. Cheng, H. Li, C. Fang, L. Ai, J. Chen, J. Su, Q. Zhang and Q. Fu, Facile synthesis of reduced graphene oxide/silver nanoparticles composites and their application for detecting heavy metal ions, *J. Alloys Compd.*, 2019, **787**, 683–693.
41 V. Tramonti, C. Lofrumento, M. R. Martina, G. Lucchesi and G. Caminati, *Nanomaterials*, 2022, 12.
42 J. K. Jose, B. Mishra, K. P. Kootery, C. T. Cherian, B. P. Tripathi, S. Sarojini and M. Balachandran, Fabrication of silver nanoparticle decorated graphene oxide membranes for water purification, antifouling and antibacterial applications, *Mater. Sci. Eng. B*, 2023, **297**, 116789.
43 S. H. Song, C.-M. Kim, M. A. Khirul, I. Ahmad, H. Jee, C. Y. Chuah, J. Park, K.-J. Chae and E. Yang, Silver nanoparticle-decorated reduced graphene oxide/nanocrystalline titanium metal-organic frameworks composite membranes with enhanced nanofiltration performance and photocatalytic ability, *Desalin. Water Treat.*, 2024, **320**, 100836.
44 A. R. Ansari, S. A. Ansari, N. Parveen, M. O. Ansari and Z. Osman, Silver Nanoparticles Embedded on Reduced Graphene Oxide@Copper Oxide Nanocomposite for High Performance Supercapacitor Applications, *Mater.*, 2021, **14**(17), 5032.
45 Z. Karami, M. Youssefi, K. Raeissi and M. Zhiani, An efficient textile-based electrode utilizing silver nanoparticles/reduced graphene oxide/cotton fabric composite for high-performance wearable supercapacitors, *Electrochim. Acta*, 2021, **368**, 137647.
46 M. Khan, M. N. Tahir, S. F. Adil, H. U. Khan, M. R. H. Siddiqui, A. A. Al-warthan and W. Tremel, Graphene based metal and metal oxide nanocomposites: synthesis, properties and their applications, *J. Mater. Chem. A*, 2015, **3**, 18753–18808.
47 C. Hu, T. Lu, F. Chen and R. Zhang, A brief review of graphene–metal oxide composites synthesis and applications in photocatalysis, *J. Chin. Adv. Mater. Soc.*, 2013, **1**, 21–39.

48 C. K. Chua and M. Pumera, Chemical reduction of graphene oxide: a synthetic chemistry viewpoint, *Chem. Soc. Rev.*, 2014, **43**, 291–312.
49 D. R. Dreyer, S. Park, C. W. Bielawski and R. S. Ruoff, The chemistry of graphene oxide, *Chem. Soc. Rev.*, 2010, **39**, 228–240.
50 B. Gurzęda, T. Buchwald, M. Nocuń, A. Bąkowicz and P. Krawczyk, Graphene material preparation through thermal treatment of graphite oxide electrochemically synthesized in aqueous sulfuric acid, *RSC Adv.*, 2017, **7**, 19904–19911.
51 S. M. S. Al-Mufti, A. Almontasser and S. J. A. Rizvi, Single and double thermal reduction processes for synthesis reduced graphene oxide assisted by a muffle furnace: A facile robust synthesis and rapid approach to enhance electrical conductivity, *AIP Adv.*, 2022, **12**, 125306.
52 M. Zainy, N. M. Huang, S. Vijay Kumar, H. N. Lim, C. H. Chia and I. Harrison, Simple and scalable preparation of reduced graphene oxide–silver nanocomposites *via* rapid thermal treatment, *Mater. Lett.*, 2012, **89**, 180–183.
53 S. Kumari, P. Sharma, S. Yadav, J. Kumar, A. Vij, P. Rawat, S. Kumar, C. Sinha, J. Bhattacharya, C. M. Srivastava and S. Majumder, A Novel Synthesis of the Graphene Oxide–Silver (GO–Ag) Nanocomposite for Unique Physiochemical Applications, *ACS Omega*, 2020, **5**, 5041–5047.
54 Q. Li and P. Hai, Rapid microwave-assisted synthesis of silver decorated-reduced graphene oxide nanoparticles with enhanced photocatalytic activity under visible light, *Mater. Sci. Semicond. Process.*, 2014, **22**, 16–20.
55 M. H. H. Ali, M. E. Goher, A. D. G. Al-Afify and S. M. El-Sayed, A facile method for synthesis rGO/Ag nanocomposite and its uses for enhancing photocatalytic degradation of Congo red dye, *SN Appl. Sci.*, 2022, **4**, 276.
56 S. Wang, Y. Zhang, H. Ma, Q. Zhang, W. Xu, J. Peng, J. Li, Z.-Z. Yu and Z. Maolin, Ionic-liquid-assisted facile synthesis of silver nanoparticle-reduced graphene oxide hybrids by gamma irradiation, *Carbon*, 2013, **55**, 245–252.
57 G. Liu, Y. Wang, X. Pu, Y. Jiang, L. Cheng and Z. Jiao, One-step synthesis of high conductivity silver nanoparticle-reduced graphene oxide composite films by electron beam irradiation, *Appl. Surf. Sci.*, 2015, **349**, 570–575.
58 Y. Liang, B. Fang, F. F. Lin and X. M. Zhu, Gamma Irradiation Assisted Synthesis of Ag/rGO Composites and their Surface Properties, *Mater. Sci. Forum*, 2017, **898**, 2224–2230.
59 M. M. Atta, M. Rabia, A. M. Elbasiony, E. O. Taha, M. M. Abdel Hamid, A. M. A. Henaish and Q. Zhang, Facile gamma-ray induced synthesis of reduced graphene oxide decorated with silver nanoparticles: a green approach for symmetric supercapacitor applications, *Fullerenes, Nanotubes Carbon Nanostruct.*, 2024, **32**, 442–451.
60 R. M. S. Jacovone, J. J. S. Soares, T. S. Sousa, F. R. O. Silva, R. H. L. Garcia, H. N. Nguyen, D. F. Rodrigues and S. K. Sakata, Antibacterial activity of silver/reduced graphene oxide nanocomposite synthesized by sustainable process, *Energy, Ecol. Environ.*, 2019, **4**, 318–324.
61 J. Belloni, M. Mostafavi, H. Remita and J.-L. Marignier, and and Marie-Odile Delcourt, Radiation-induced synthesis of mono- and multi-metallic clusters and nanocolloids, *New J. Chem.*, 1998, **22**, 1239–1255.
62 J. Belloni and M. Mostafavi, Radiation chemistry of nanocolloids and clusters, *Stud. Phys. Theor. Chem.*, 2001, **87**, 411–452.
63 J. Belloni and M. Mostafavi, *Metal Clusters in Chemistry*, 1999, pp. 1213–1247.
64 Y. Benguedouar, N. Keghouche and J. Belloni, Structural and magnetic properties of Ni–Pt nanoalloys supported on silica, *Mater. Sci. Eng., B*, 2012, **177**, 27–33.
65 H. Remita, J. Khatouri, M. Tréguer, J. Amblard and J. Belloni, Silver-palladium alloyed clusters synthesized by radiolysis, *Z. Phys. D: At., Mol. Clusters*, 1997, **40**, 127–130.
66 M. Tréguer, C. de Cointet, H. Remita, J. Khatouri, M. Mostafavi, J. Y. Amblard, J. Belloni and R. De Keyzer, Dose Rate Effects on Radiolytic Synthesis of Gold-Silver Bimetallic Clusters in Solution, *J. Phys. Chem. B*, 1998, **102**, 4310–4321.
67 T. Bahry, B. Khurshid, Y. Chouli, S. Abou Zeid, C. Sollogoub, M. Gervais, T. T. Bui, F. Goubard and S. Remita, Gamma rays as innovative tool towards synthesizing conducting copolymers with improved properties, *New J. Chem.*, 2021, **45**, 13142–13157.
68 C. Zhenpeng, C. Coletta, T. Bahry, J.-L. Marignier, J.-M. Guigner, M. Gervais, S. Baiz, F. Goubard and S. Remita, A novel radiation chemistry-based methodology for the synthesis of PEDOT/Ag nanocomposites, *Mater. Chem. Front.*, 2017, **1**, 879–892.
69 L. Hu, S. Abou Zeid, A. Bistintzanos, S. Khaoulani, D. Dragoe, R. Ghasemi, F. Muller, M. Gervais, C. Sollogoub, M. Goldmann and S. Remita, One-pot radiolytically synthesized reduced graphene oxide-gold nanoparticles composites and exploration in energy storage, *Appl. Surf. Sci.*, 2024, **678**, 161109.
70 G. G. Flores-Rojas, F. López-Saucedo and E. Bucio, Gamma-irradiation applied in the synthesis of metallic and organic nanoparticles: A short review, *Radiat. Phys. Chem.*, 2020, **169**, 107962.
71 H. Fricke and S. Morse, The chemical action of roentgen rays on dilute ferrosulphate solutions as a measure of dose, *Am. J. Roentgenol., Radium Ther. Nucl. Med.*, 1927, **18**, 430–432.
72 E. J. Hart and H. Fricke, Chemical dosimetry, *Radiat. Dosim.*, 1967, **2**, 167–239.
73 S. Remita, Effet de ligands sur les propriétés thermodynamiques, cinétiques et spectrales d'agrégats métalliques synthétisés par radiolyse, Thèse de doctorat de l'Université Paris-sud, Paris sud XI, 1995.
74 M. Von Piechowski, M.-A. Thelen, J. Hoigné and R. E. Bühler, tert-Butanol as an OH-Scavenger in the Pulse Radiolysis of Oxygenated Aqueous Systems, *Ber. Bunsenges. Phys. Chem.*, 1992, **96**, 1448–1454.
75 A. Henglein, J. W. T. Spinks. and R. J. Woods, An Introduction to Radiation Chemistry, Third Edition, John-Wiley

and Sons, Inc., New York, Toronto 1990. ISBN 0-471-61403-3. 574 Seiten, Preis: DM 91, 45., *Ber. Bunsenges. Phys. Chem.*, 1991, **95**, 451.

76 E. Janata, A. Henglein and B. G. Ershov, First Clusters of Ag+ Ion Reduction in Aqueous Solution, *J. Phys. Chem.*, 1994, **98**, 10888–10890.

77 J. Belloni, Nucleation, growth and properties of nanoclusters studied by radiation chemistry: Application to catalysis, *Catal. Today*, 2006, **113**, 141–156.

78 A. Kahnt, R. Flyunt, C. Laube, W. Knolle, S. Eigler, R. Hermann, S. Naumov and B. Abel, How fast is the reaction of hydrated electrons with graphene oxide in aqueous dispersions?, *Nanoscale*, 2015, **7**, 19432–19437.

79 J. Pukies, W. Roebke and A. Henglein, Pulsradiolytische Untersuchung einiger Elementarprozesse der Silberreduktion, *Ber. Bunsenges. Phys. Chem.*, 1968, **72**, 842–847.

80 K. P. Madden and S. P. Mezyk, Critical Review of Aqueous Solution Reaction Rate Constants for Hydrogen Atoms, *J. Phys. Chem. Ref. Data*, 2011, **40**, 23103.

81 J. Tauc, R. Grigorovici and A. Vancu, Optical Properties and Electronic Structure of Amorphous Germanium, *Phys. Status Solidi*, 1966, **15**, 627–637.

82 X. Zhang and Ø. Mikkelsen, Graphene Oxide/Silver Nanocomposites as Antifouling Coating on Sensor Housing Materials, *J. Cluster Sci.*, 2022, **33**, 627–635.

83 T. Tsuji, K. Iryo, N. Watanabe and M. Tsuji, Preparation of silver nanoparticles by laser ablation in solution: influence of laser wavelength on particle size, *Appl. Surf. Sci.*, 2002, **202**, 80–85.

84 C. J. Murphy and N. R. Jana, Controlling the Aspect Ratio of Inorganic Nanorods and Nanowires, *Adv. Mater.*, 2002, **14**, 80–82.

85 O. Wilson, G. J. Wilson and P. Mulvaney, Laser Writing in Polarized Silver Nanorod Films, *Adv. Mater.*, 2002, **14**, 1000–1004.

86 S. Gurunathan, J. W. Han, A. A. Dayem, V. Eppakayala and J.-H. Kim, Oxidative stress-mediated antibacterial activity of graphene oxide and reduced graphene oxide in Pseudomonas aeruginosa, *Int. J. Nanomed.*, 2012, **7**, 5901–5914.

87 S. Liu, J. Tian, L. Wang, H. Li, Y. Zhang and X. Sun, Stable Aqueous Dispersion of Graphene Nanosheets: Noncovalent Functionalization by a Polymeric Reducing Agent and Their Subsequent Decoration with Ag Nanoparticles for Enzymeless Hydrogen Peroxide Detection, *Macromolecules*, 2010, **43**, 10078–10083.

88 J. Li and C. Liu, Ag/Graphene Heterostructures: Synthesis, Characterization and Optical Properties, *Eur. J. Inorg. Chem.*, 2010, 1244–1248.

89 A. F. de Faria, D. S. T. Martinez, S. M. M. Meira, A. C. M. de Moraes, A. Brandelli, A. G. S. Filho and O. L. Alves, Antiadhesion and antibacterial activity of silver nanoparticles supported on graphene oxide sheets, *Colloids Surf., B*, 2014, **113**, 115–124.

90 A. Aziz, M. Khalid, M. Saeed Akhtar, M. Nadeem, Z. Gilani, M. Khan, J. Rehman, Z. Ullah and M. Saleem, Structural, morphological and optical investigations of silver nanoparticles synthesized by sol–gel auto-combustion method, *Digest J. Nanomater. Biostruct.*, 2018, **13**, 679–683.

91 S. Gasaymeh, S. Radiman, L. Yook Heng, E. Saion and M. Saeed, Synthesis and Characterization of Silver/Polyvinilpirrolidone (Ag/PVP) Nanoparticles Using Gamma Irradiation Techniques, *Am. J. Appl. Sci.*, 2010, **7**, 892–901.

92 D. M. Ikram, A. Raza, M. Imran, A. Ul-Hamid and S. Ali, Hydrothermal Synthesis of Silver Decorated Reduced Graphene Oxide (rGO) Nanoflakes with Effective Photocatalytic Activity for Wastewater Treatment, *Nanoscale Res. Lett.*, 2020, **15**, 95.

93 A. Das, R. Kumar, S. Goutam and S. Sagar, Sunlight Irradiation Induced Synthesis of Silver Nanoparticles using Glycolipid Bio-surfactant and Exploring the Antibacterial Activity, *J. Bioeng. Biomed. Sci.*, 2016, **6**, 208.

94 J. Hölzl and F. K. Schulte, in *Solid Surface Physics*, ed. J. Hölzl, F. K. Schulte and H. Wagner, Springer Berlin Heidelberg, Berlin, Heidelberg, 1979, pp. 1–150.

95 H. Lüth, *Solid Surfaces, Interfaces and Thin Films*, 6th edn, 2015.

96 D. P. Woodruff, *Modern Techniques of Surface Science*, Cambridge University Press, 1994.

97 N. W. Ashcroft and N. D. Mermin, *Physique des solides*, 1st édn, 2012.

98 A. L. Dadlani, P. Schindler, M. Logar, S. P. Walch and F. B. Prinz, Energy States of Ligand Capped Ag Nanoparticles: Relating Surface Plasmon Resonance to Work Function, *J. Phys. Chem. C*, 2014, **118**, 24827–24832.

99 P. Lozovskis, V. Jankauskaitė, A. Guobienė, V. Kareivienė and A. Vitkauskienė, Effect of Graphene Oxide and Silver Nanoparticles Hybrid Composite on P. aeruginosa Strains with Acquired Resistance Genes, *Int. J. Nanomed.*, 2020, **15**, 5147–5163.

100 D. I. Rodríguez-Otamendi, V. Meza-Laguna, D. Acosta, E. Álvarez-Zauco, L. Huerta, V. A. Basiuk and E. V. Basiuk, Eco-friendly synthesis of graphene oxide–silver nanoparticles hybrids: The effect of amine derivatization, *Diamond Relat. Mater.*, 2021, **111**, 108208.

101 A. Shaikh, S. Parida and S. Böhm, One step eco-friendly synthesis of Ag-Reduced graphene oxide nanocomposite by phytoreduction for sensitive nitrite determination, *RSC Adv.*, 2016, **6**, 100383.

102 S. T. Jackson and R. G. Nuzzo, Determining hybridization differences for amorphous carbon from the XPS C 1s envelope, *Appl. Surf. Sci.*, 1995, **90**, 195–203.

103 D. Bourgoin, S. Turgeon and G. G. Ross, Characterization of hydrogenated amorphous carbon films produced by plasma-enhanced chemical vapour deposition with various chemical hybridizations, *Thin Solid Films*, 1999, **357**, 246–253.

104 A. Siokou, F. Ravani, S. Karakalos, O. Frank, M. Kalbac and C. Galiotis, Surface refinement and electronic properties of graphene layers grown on copper substrate: An XPS, UPS and EELS study, *Appl. Surf. Sci.*, 2011, **257**, 9785–9790.

105 N. Minh Dat, V. N. P. Linh, L. A. Huy, N. T. Huong, T. H. Tu, N. T. L. Phuong, H. M. Nam, M. Thanh Phong

and N. H. Hieu, Fabrication and antibacterial activity against Pseudomonas aeruginosa and Staphylococcus aureus of silver nanoparticle decorated reduced graphene oxide nanocomposites, *Mater. Technol.*, 2019, **34**, 369–375.

106 V. H. Le, T. H. Nguyen, H. H. Nguyen, L. T. N. Huynh, A. Le Vo, T. K. T. Nguyen, D. T. Nguyen and V. Q. Lam, Fabrication and Electrochemical Behavior Investigation of a Pt-Loaded Reduced Graphene Oxide Composite (Pt@rGO) as a High-Performance Cathode for Dye-Sensitized Solar Cells, *Int. J. Photoenergy*, 2020, **2020**, 8927124.

107 B. Fan, H. Guo, J. Shi, C. Shi, Y. Jia, H. Wang, D. Chen, Y. Yang, H. Lu and R. Zhang, Facile One-Pot Preparation of Silver/Reduced Graphene Oxide Nanocomposite for Cancer Photodynamic and Photothermal Therapy, *J. Nanosci. Nanotechnol.*, 2016, **16**, 7049–7054.

108 S. Gurunathan, J. Han, J.-H. Park, E. Kim, Y. Choi, D.-N. Kwon and J.-H. Kim, Reduced graphene oxide-silver nanoparticle nanocomposite: A potential anticancer nanotherapy, *Int. J. Nanomed.*, 2015, **10**, 6257–6276.

109 N. B. Tadesse, D. Meshesha and K. Basavaiah, Green syntheses of silver nanoparticle decorated reduced graphene oxide using L-methionine as a reducing and stabilizing agent for enhanced catalytic hydrogenation of 4-nitrophenol and antibacterial activity, *RSC Adv.*, 2019, **9**, 39264–39271.

110 N. M. S. Hidayah, W.-W. Liu, C.-W. Lai, N. Z. Noriman, C.-S. Khe, U. Hashim and H. C. Lee, Comparison on graphite, graphene oxide and reduced graphene oxide: Synthesis and characterization, *AIP Conf. Proc.*, 2017, **1892**, 150002.

111 M. Yu, C. Qin, Z. Yu, B. Sun, D. Ni, D. Zhang and P. Liang, Synergetic enhancement effet of Ag/rGO as SERS platform for capture and trace detection of fenvalerate molecules, *Chemosensors*, 2024, **12**(5), 82.

112 N. S. A. Aziz, M. K. N. Azmi and A. M. Bin Hashim, One-pot green synthesis of highly reduced graphene oxide decorated with silver nanoparticles, *Sains Malays.*, 2017, **46**, 1083–1088.

113 J. Tian, S. Liu, Y. Zhang, H. Li, L. Wang, Y. Luo, A. M. Asiri, A. O. Al-Youbi and X. Sun, Environmentally friendly, one-pot synthesis of Ag nanoparticle-decorated reduced graphene oxide composites and their application to photocurrent generation, *Inorg. Chem.*, 2012, **51**, 4742–4746.

114 M. Y. Wang, T. Shen, M. Wang, D. Zhang and J. Chen, One-pot green synthesis of Ag nanoparticles-decorated reduced graphene oxide for efficient nonenzymatic H_2O_2 biosensor, *Mater. Lett.*, 2013, **107**, 311–314.

115 T. Jiao, H. Guo, Q. Zhang, Q. Peng, Y. Tang, X. Yan and B. Li, Reduced Graphene Oxide-Based Silver Nanoparticle-Containing Composite Hydrogel as Highly Efficient Dye Catalysts for Wastewater Treatment, *Sci. Rep.*, 2015, **5**, 11873.

116 K. Garg, P. Papponen, A. Johansson, N. Puttaraksa and L. Gilbert, Preparation of graphene nanocomposites from aqueous silver nitrate using graphene oxide's peroxidase-like and carbocatalytic properties, *Sci. Rep.*, 2020, **10**, 5126.

117 S. Chanarsa, J. Jakmunee and K. Ounnunkad, A Bifunctional Nanosilver-Reduced Graphene Oxide Nanocomposite for Label-Free Electrochemical Immunosensing, *Front. Chem.*, 2021, **9**, 631571.

118 I. Roy, D. Rana, G. Sarkar, A. Bhattacharyya, N. Saha, S. Mondal, S. Pattanayak, S. Chattopadhyay and D. Chattopadhyay, Physical and electrochemical characterization of reduced graphene oxide/silver nanocomposites synthesized by adopting green approach, *RSC Adv.*, 2015, **5**, 25357–25364.

119 P. Garg, R.K. Bharti, R. Soni and R. Raman, Graphene oxide–silver nanocomposite SERS substrate for sensitive detection of nitro explosives, *J. Mater. Sci. Mater. Electron.*, 2020, **31**, 1094–1104.

120 A. Koutsioukis, K. Vrettos, V. Belessi and V. Georgakilas, Conductivity Enhancement of Graphene and Graphene Derivatives by Silver Nanoparticles, *Appl. Sci.*, 2023, **13**, 7600.

121 H. Kolya, T. Kuila, N. H. Kim and J. H. Lee, Bioinspired silver nanoparticles/reduced graphene oxide nanocomposites for catalytic reduction of 4-nitrophenol, organic dyes and act as energy storage electrode material, *Composites, Part B*, 2019, **173**, 106924.

122 N. Devi, S. Sinha, I. Wahengbam, S. Nongthombam and B. Swain, Silver-decorated reduced graphene oxide nanocomposite for supercapacitor electrode application, *Bull. Mater. Sci.*, 2021, **45**, 1–11.

123 H. Quan, Y. Shao, C. Hou, Q. Zhang, H. Wang and Y. Li, Room-temperature synthesis of 3-dimensional Ag-graphene hybrid hydrogel with promising electrochemical properties, *Mater. Sci. Eng., B*, 2013, **178**, 769–774.

124 Y. Zhang, S. Wang, L. Li, K. Zhang, J. Qiu, M. Davis and L. J. Hope-Weeks, Tuning electrical conductivity and surface area of chemically-exfoliated graphene through nanocrystal functionalization, *Mater. Chem. Phys.*, 2012, **135**, 1057–1063.

125 K. S. Lau, S. T. Tan, R. T. Ginting, P. S. Khiew, S. X. Chin and C. H. Chia, A mechanistic study of silver nanostructure incorporating reduced graphene oxide *via* a flow synthesis approach, *New J. Chem.*, 2020, **44**, 1439–1445.